

# Smart Kanata: A Framework for Autonomous Decision Making in Rapid Follow-up Observations of Cataclysmic Variables

Makoto UEMURA,<sup>1,\*</sup> Yuzuki KOGA,<sup>2</sup> Ryosuke SAZAKI,<sup>2</sup> Tomoya YUKINO,<sup>3,4</sup> Tatsuya NAKAOKA,<sup>1</sup> Ryo IMAZAWA,<sup>2</sup> Taichi KATO,<sup>5</sup> Daisaku NOGAMI,<sup>5</sup> Keisuke ISOGAI,<sup>5,6</sup> Naoto KOJIGUCHI,<sup>5</sup> Kenta TAGUCHI,<sup>5</sup> Yusuke TAMPO,<sup>5,7,8</sup> Hiroyuki MAEHARA,<sup>9</sup> and Shiro IKEDA<sup>10</sup>

<sup>1</sup>Hiroshima Astrophysical Science Center, Hiroshima University, Kagamiyama 1-3-1, Higashi-Hiroshima, Hiroshima 739-8526, Japan

<sup>2</sup>Department of Physics, Graduate School of Advanced Science and Engineering, Hiroshima University, 1-3-1 Kagamiyama, Higashi-Hiroshima, Hiroshima 739-8526, Japan

<sup>3</sup>Institute of Astronomy, Graduate School of Science, The University of Tokyo, 2-21-1 Osawa, Mitaka, Tokyo 181-0015, Japan

<sup>4</sup>Department of Astronomy, Graduate School of Science, The University of Tokyo, Hongo 7-3-1, Bunkyo-ku, Tokyo 113-0033, Japan

<sup>5</sup>Department of Astronomy, Kyoto University, Kitashirakawa-Oiwake-cho, Sakyo-ku, Kyoto, Kyoto 606-8502, Japan

<sup>6</sup>Department of Multi-Disciplinary Sciences, Graduate School of Arts and Sciences, The University of Tokyo, 3-8-1 Komaba, Meguro, Tokyo 153-8902, Japan

<sup>7</sup>South African Astronomical Observatory, PO Box 9, Observatory, 7935, Cape Town, South Africa

<sup>8</sup>Department of Astronomy, University of Cape Town, Private Bag X3, Rondebosch 7701, South Africa

<sup>9</sup>Subaru Telescope Okayama Branch Office, National Astronomical Observatory of Japan, National Institutes of Natural Sciences, 3037-5 Honjo, Kamogata-cho, Asakuchi, Okayama 719-0232, Japan

<sup>10</sup>The Institute of Statistical Mathematics, 10-3 Midori-cho, Tachikawa, Tokyo 190-8562, Japan

\*E-mail: uemuram@hiroshima-u.ac.jp

ORCID: 0000-0002-7375-7405

## Abstract

Studying the early stages of transient events provides crucial information about the fundamental physical processes in cataclysmic variables (CVs). However, determining an appropriate observation mode immediately after the discovery of a new transient presents challenges due to significant uncertainties regarding its nature. We developed a framework designed for autonomous decision making in prompt follow-up observations of CVs using the Kanata 1.5-m telescope. The system, named Smart Kanata, first estimates the class probabilities of variable star types using a generative model. It then selects the optimal observation mode from three possible options based on the mutual information calculated from the class probabilities. We have operated the system for  $\sim 300$  days and obtained 21 samples, among which automated observations were successfully performed for a nova and a microlensing event. In the time-series spectra of the nova V4370 Oph, we detected a rapid deepening of the absorption component of the  $H\alpha$  line. These initial results demonstrate the capability of Smart Kanata in facilitating rapid observations and improving our understanding of outbursts and eruptions of CVs and other galactic transients.

**Keywords:** accretion, accretion disks — methods: observational — stars: dwarf novae — novae, cataclysmic variables

## 1 Introduction

Cataclysmic variables (CVs) are close binary systems in which a white dwarf experiences accretion from a companion star that fills its Roche lobe (for a review, see Warner 1995). This accretion process results in transient phenomena, including nova eruptions and dwarf nova outbursts. Uninterrupted observations spanning the entire duration of these phenomena are essential to understand them. However, capturing the initial phase, particularly the rapidly rising phase, presents challenges due to its short time-scale of less than 1 day. Exploring the initial stage of transients, typically characterized by an unsteady transitional state, provides valuable insights into their underlying physical models.

In novae, the accretion triggers a runaway thermonuclear burst

on the surface of the white dwarf. This burst leads to the ejection of accumulated matter, making a photosphere that envelops the entire binary star system (for a recent review, see Della Valle, Izzo 2020). The dynamic formation and subsequent evolution of the ejecta have recently been investigated through spectroscopic observations conducted during the initial stages of nova eruptions. In the pioneering work of Arai et al. (2015), an optical spectrum was acquired within an extremely early temporal window, specifically at 0.19 days following the initial detection of the nova eruption in T Pyx. This spectrum exhibited distinct features reminiscent of Wolf-Rayet stars, including N v, IV, C IV and He II emission lines, which were unprecedented for novae. In particular, these highly excited lines disappeared within 2 days. A similar spectrum was identified during the rising phase of Gaia22alz (Aydi et al. 2023)

and V1405 Cas (Taguchi et al. 2023). Even in ordinary emission lines, Yamanaka et al. (2010) detected the rapid evolution of high-velocity components within the first day of the nova eruption in U Sco. These observations indicate the presence of previously uncharacterized conditions in the early phases of nova eruptions, suggesting that further investigation is needed to understand the underlying mechanisms.

Dwarf novae exhibit a repetitive pattern of outbursts that are triggered by the thermal instability of the accretion disk (Osaki 1996). Within the category of dwarf novae, WZ Sge-type stars exhibit distinctive features: large outburst amplitudes ( $\sim 8$  mag), long recurrence time ( $\sim 10$  yr), and the emergence of early superhumps during the initial week of their outburst (Howell et al. 1995; Kato 2015). The early superhumps are short-term periodic fluctuations characterized by a doubly-peaked profile of the orbital period. They arise from geometric irregularities within the disk structure. However, the underlying mechanism responsible for the disk structure remains poorly understood. WZ Sge stars have the most extreme binary mass ratio ( $M_2/M_1 \lesssim 0.1$ ) among CVs. Consequently, the accretion disk in these systems is expected to approach the 2:1 resonance radius. At this radius, tidal dissipation would influence the disk structure (Osaki, Meyer 2002). This scenario emphasizes the importance of early superhumps for studying the tidal effect in accretion disks in binary systems with extreme mass ratios.

In the case of both novae and dwarf novae, it is necessary to observe the very early stages of the transient event to understand the aforementioned phenomena. The appropriate mode of the follow-up observation depends on the nature of the transient. For instance, photometric observations are employed to identify early superhumps, while spectroscopic observations are used to investigate the formation process of the nova ejecta. Unlike objects such as supernovae, where spectroscopic observations are consistently prioritized for follow-up, the availability of this diverse selection complicates immediate follow-up observations of CVs. Determining the suitable observation mode for a new transient is a challenging task because of the limited information available, leading to substantial uncertainties in its nature immediately after its discovery. This decision-making process has traditionally been the responsibility of experts in CVs; however, there exists a risk of overlooking critical phases of the event without the guidance of these experts during nighttime observations.

Another problem arises from the substantial increase in the count of transient events suitable for potential follow-up observation due to large survey projects in recent years (e.g. ASAS-SN in Jayasinghe et al. 2018; Zwicky Transient Facility in Bellm et al. 2019). The use of manual decision making by experts has become constrained as a result of this increase.

In this paper, we present a framework designed for the autonomous decision-making process in rapid follow-up observations of CVs using the Kanata 1.5-m telescope at the Higashi-Hiroshima Observatory. We call this system Smart Kanata. The novelty of our Smart Kanata as an observation system is that it automatically determines and executes the observation expected to have the largest information gain using the framework of information theory, rather than simply automatically executing a predetermined observation.

Previous studies have explored machine learning techniques for classifying transient events and variable stars (for a review, see Förster et al. 2021). However, most existing models are designed for broad classifications of variable star types or focus exclusively on particular types, such as supernovae (e.g., Muthukrishna et al.

2019) and pulsating variables (e.g., Jayasinghe et al. 2019). In contrast, our study targets finer classifications of CVs, including subtypes of dwarf novae, necessitating the development of a new and specialized classification model.

The automation of observations, from the detection of transient events to their follow-up, has advanced significantly, particularly in studies of gamma-ray bursts and supernovae (e.g., Gal-Yam et al. 2011). These automated systems have made substantial contributions to our understanding of such phenomena; however, they often rely on static decision trees or predefined observation priorities. Mahabal et al. (2008) and Djorgovski et al. (2011) introduced the concept of using probabilistic models for dynamic, autonomous decision-making processes to determine the optimal observation mode. Building on this approach, our study implements it within an observational system and demonstrates its effectiveness in real-time follow-up of CVs.

The structure of this paper is as follows: Section 2 provides a comprehensive description of the system. Section 3 presents the initial results observed during the 11-month period from December 2023 to October 2024. In Section 4, we discuss the performance of the system, particularly the classifier, and the implications of the acquired data. Finally, Section 5 offers a summary of our findings.

## 2 The Smart Kanata system

In Smart Kanata, we classify objects into five categories: nova (class N), dwarf nova (class DN), WZ Sge-type dwarf nova (class WZ), mira (class M), and flare star (class F). The latter two classes are included because they are sometimes mistaken for transient phenomena in CVs. We use eight features for each sample: the galactic coordinates ( $\ell$  and  $b$ ), the absolute magnitudes at maximum brightness ( $M_{\max}$ ) and in quiescence ( $M_{\text{qui}}$ ), the transient amplitude ( $a$ ), and the quiescent colors ( $g-r$ ,  $r-i$ , and  $i-z$ ). The goal of Smart Kanata is to select the optimal follow-up observation mode for use with the Kanata telescope. We consider three available observation modes: multiband imaging to obtain the  $B-V$  color index (mode  $B-V$ ), spectroscopy to measure the equivalent width of  $H\alpha$  (mode EW), and time-series imaging to investigate short-term periodic variations (mode Var).

The Smart Kanata system monitors new transients from online services to find potential targets suitable for observation using the Kanata telescope (§2.1). Upon detecting a candidate target, Smart Kanata classifies the object and selects the optimal observation mode. We introduce the framework of these processes in §2.2. Details about the classifier and the decision-making process for observations are described in §2.3 and §2.4, respectively. Once the decision is made, the system initiates automated observations, as explained in §2.5.

### 2.1 Target selection

The Smart Kanata system monitors online platforms for new transients. These platforms include the Transient Name Server (TNS)<sup>1</sup>, CBAT's "Transient Objects Confirmation Page" (TOCP)<sup>2</sup>, ASAS-SN Transients (Jayasinghe et al. 2018), and ANTARES (Matheson et al. 2021). Our system identifies transients that are brighter than a certain limit ( $m_{\text{lim}}$ ) and are detected within a defined temporal window ( $\Delta t_{\text{dis}}$ ). Detailed parameter values are provided in Table 1.

<sup>1</sup> <https://www.wis-tns.org>

<sup>2</sup> <http://www.cbat.eps.harvard.edu/unconf/tocp.html>

After the system identifies transients, it verifies if they correspond to either recognized variable stars or active galactic nuclei (AGN) listed in the available database. Our search for recognized variable stars involves referencing the AAVSO VSX catalog (Watson et al. 2006), the ATLAS catalog (Heinze et al. 2018), and the ASAS-SN catalog (Jayasinghe et al. 2018). For identifying known AGN, we consult the WISE AGN candidates (Assef et al. 2018), AGNs detected in the mid-infrared (MIR) through AllWISE data (Secrest et al. 2015), Blazar Radio and Optical Survey (Itoh et al. 2020), and the FIRST-NVSS-SDSS AGN sample catalog (Smolčić 2009). The system identifies new transients as known sources if they fall within a distance of  $r_{\text{match}}$  from their position. The default value for  $r_{\text{match}}$  is  $2''.0$ , as shown in Table 1.

We excluded clear supernovae (SNe) from our target candidates. We identify such SNe as events whose host galaxy is listed in the online services. In addition, we consider an event with a neighboring galaxy to be a potential supernova, and exclude it. The neighboring galaxy is identified as a galaxy within a distance of  $r_{\text{gal}}$  from the event's position in the NGC 2000.0 Catalogue (Sinnott 1988), SDSS-DR8 galaxies categorized by WND-CHARM (Kuminski, Shamir 2016), or the GLADE v2.3 catalog (Dályá et al. 2018). The default value for  $r_{\text{gal}}$  is set to  $10''.0$ , as shown in Table 1.

The observation sequence is initiated if a new transient event is identified with a known nova or WZ Sge-type dwarf nova in the AAVSO VSX catalog, as detailed in § 2.4. If the event is not found in the aforementioned catalogs and is not identified as a SN, we then initiate the classification and subsequent decision-making sequences described in § 2.2 and 2.3, respectively.

## 2.2 Uncertainty of the class and choosing the follow-up observation mode

Smart Kanata uses probabilistic models for the classification of transients and the selection of follow-up observation modes. Here, we describe the mathematical framework.

Let  $\pi(k)$  be the initial guess, or in the Bayesian statistical term, the prior distribution of the transient class, where  $k$  represents the class,  $\sum_k \pi(k) = 1$ , and  $\pi(k) \geq 0$  for all  $k$ . When a new transient is detected, a feature vector, which we denote as  $\mathbf{x}$ , is provided. Assuming the probability distribution  $p(\mathbf{x}|k)$  is known for each class, the posterior distribution of the class is computed with the Bayes theorem as in the following equation, and the class with the maximum probability is the estimated class.

$$p_{\mathbf{x}}(k) := p(k|\mathbf{x}) = \frac{p(\mathbf{x}|k)\pi(k)}{\sum_k p(\mathbf{x}|k)\pi(k)}. \quad (1)$$

The classification is certain if the probability of one class is much larger than that of the others; otherwise, it is not. The uncertainty of the classification is well represented by the Shannon entropy:

$$H_{\mathbf{x}}(K) = - \sum_k p_{\mathbf{x}}(k) \log_2 p_{\mathbf{x}}(k). \quad (2)$$

The unit of the Shannon entropy is bits. The entropy is maximized to  $\log_2 5$  when the class is totally unknown ( $p_{\mathbf{x}}(k) = 1/5$ ), and minimized to 0 when the class is known ( $p_{\mathbf{x}}(k) = 1$  for one of the classes).

When a transient is detected, the uncertainty regarding its classification is typically high because the information obtained from  $\mathbf{x}$  is limited. In order to achieve a certain classification, making an appropriate follow-up observation is crucial. The strategy of Smart Kanata is to choose the follow-up observation mode that will minimize the uncertainty.

Let  $m$  denote the possible mode of the follow-up observation. For each mode, we define a measurement  $y_m$ . This is a virtual measurement because the real measurement is obtained after the follow-up observation is executed. Again, we assume the probability distribution  $q(y_m|k)$  is known for each class and each observation mode.

Suppose a follow-up observation mode  $m$  is chosen and a virtual measurement  $y_m$  is observed, the posterior distribution and the Shannon entropy is defined as follows:

$$q_{\mathbf{x}}(k|y_m) := q(k|y_m, \mathbf{x}) = \frac{q_{\mathbf{x}}(k, y_m)}{q_{\mathbf{x}}(y_m)} = \frac{q(y_m|k)p_{\mathbf{x}}(k)}{\sum_k q(y_m|k)p_{\mathbf{x}}(k)} \quad (3)$$

$$H_{\mathbf{x}}(K|y_m) = - \sum_k q_{\mathbf{x}}(k|y_m) \log_2 q_{\mathbf{x}}(k|y_m). \quad (4)$$

Here, we defined  $q_{\mathbf{x}}(k, y_m) := q(k, y_m|\mathbf{x})$  and  $q_{\mathbf{x}}(y_m) := q(y_m|\mathbf{x})$ .

The expected value of  $H_{\mathbf{x}}(K|y_m)$ , known as the conditional entropy, is calculated as follows:

$$\begin{aligned} H_{\mathbf{x}}(K|Y_m) &= \int q_{\mathbf{x}}(y_m) H_{\mathbf{x}}(K|y_m) dy_m \\ &= - \int \sum_k q_{\mathbf{x}}(k, y_m) \log_2 \frac{q_{\mathbf{x}}(k, y_m)}{q_{\mathbf{x}}(y_m)} dy_m. \end{aligned} \quad (5)$$

It is easy to show that  $H_{\mathbf{x}}(K) \geq H_{\mathbf{x}}(K|Y_m)$  holds in general. The difference between  $H_{\mathbf{x}}(K)$  and  $H_{\mathbf{x}}(K|Y_m)$  is called the mutual information (MI) in information theory.

$$\begin{aligned} I_{\mathbf{x}}(K; Y_m) &= H_{\mathbf{x}}(K) - H_{\mathbf{x}}(K|Y_m) \\ &= \int \sum_k q_{\mathbf{x}}(k, y_m) \log_2 \frac{q_{\mathbf{x}}(k, y_m)}{q_{\mathbf{x}}(y_m)p_{\mathbf{x}}(k)} dy_m \end{aligned} \quad (6)$$

This is nonnegative and defines the expected gain of the information by choosing the observation mode  $m$ . Smart Kanata chooses the most informative observation mode, that is, the mode  $m$  which maximizes  $I_{\mathbf{x}}(K; Y_m)$  (or equivalently, minimizes  $H_{\mathbf{x}}(K|Y_m)$ ).

This framework requires probability models  $\pi(k)$ ,  $p(\mathbf{x}|k)$ , and  $q(y_m|k)$ . We explain how we defined them in the next subsections.

## 2.3 Variable star type classification

We develop a generative model (GM) that estimates  $p_{\mathbf{x}}(k)$  by modeling  $\pi(k)$  and  $p(\mathbf{x}|k)$  in equation (1).

For the prior probability  $\pi(k)$  in Equation (1), we assume a flat distribution:  $\pi(k) = (0.2, 0.2, 0.2, 0.2, 0.2)$ . Ideally, this prior distribution should reflect the distribution of real targets in Smart Kanata. However, estimating the distribution based on the population of each class of variables is challenging, as the actual samples are generated through the complex detection processes of various surveys. The prior distribution will be updated as the number of actual samples increases during the operation of Smart Kanata.

We approximate  $p(\mathbf{x}|k)$  as multivariate normal distributions, given by:

$$p(\mathbf{x}|k) = \frac{1}{\sqrt{(2\pi)^N |\Sigma_k|}} \exp \left\{ -\frac{1}{2} (\mathbf{x} - \boldsymbol{\mu}_k)^T \Sigma_k^{-1} (\mathbf{x} - \boldsymbol{\mu}_k) \right\}, \quad (7)$$

where  $N$  represents the number of features,  $\boldsymbol{\mu}_k$  is the mean of the feature vector, and  $\Sigma_k$  represents the covariance matrix of the features for class  $k$ , with dimensions  $N \times N$ . These model parameters,  $\boldsymbol{\mu}_k$  and  $\sigma_{ij}$  (the elements of  $\Sigma$ ) can be estimated as the mean of the sample and the variance/covariance of the sample from the training data sets described in the following.

We collected the training dataset samples from the AAVSO VSX based on the object types as follows:

**Table 1.** System parameters of Smart Kanata.

Parameter	Meaning	Value
$m_{\text{lim}}$	Magnitude limit for faint objects to be extracted	16.0
$\Delta t_{\text{dis}}$	Elapsed time since discovery to be extracted	2.0 d
$r_{\text{match}}$	Radius to search for the counterpart of the object.	2''.0
$r_{\text{gal}}$	Radius to search for the galaxy near the object	10''.0
$p(k)$	Prior probability for the classifier	(0.2, 0.2, 0.2, 0.2, 0.2)
$p_{\text{obs}}$	Threshold of class probability to initiate observations	0.95
$p_{\text{target}}$	Threshold of class N or WZ probability to initiate observations	0.10

**Class N** Labeled N, NA, NB, NC, and NR.

**Class DN** Labeled UGSS, UGZ, UGSU, and UGER.

**Class WZ** Labeled UGWZ.

**Class M** Labeled M.

**Class F** Labeled UV.

For all classes, we specifically collected objects with recorded magnitudes at maximum ( $m_{\text{max}}$ ) in the pass-bands  $V$ ,  $CV$ ,  $g$ , or  $pg$ . We excluded AM CVn stars from our data set because their quiescent color and outburst amplitude have distinct distributions from those of ordinary dwarf novae (Solheim 2010). Extragalactic objects were also excluded. Additionally, to ensure a more evenly distributed dataset, we omitted class M objects discovered by OGLE to avoid excessive concentration in the bulge direction (Groenewegen, Blommaert 2005; Matsunaga et al. 2005). Furthermore, we only included long-period Class M objects with periods exceeding 400 days, as they could be confused with CVs. We exclusively extracted bright Class F objects with  $m_{\text{max}} < 16.0$  to obtain magnitude and color information for their quiescent counterparts.

We obtain  $\ell$ ,  $b$  and  $m_{\text{max}}$  from the coordinates and the magnitude at the time of discovery for new transients. For our training dataset, we rely on AAVSO VSX, which provides these features for all the samples. We calculate  $M_{\text{max}}$  if we have access to the distance ( $d$ ) information from Gaia DR3, without adjusting for interstellar extinction (Gaia Collaboration et al. 2023). To determine the apparent magnitude at quiescence,  $m_{\text{qui}}$ , we use the  $G$ -band mag. from Gaia DR3 whenever available. If not, we consider alternative sources in the following order:  $g$  mag. from Pan-STARRS Release 1 Survey (DR1),  $g$  mag. from Sloan Digital Sky Surveys (SDSS) Release 16 (DR16),  $r$  mag. from Pan-STARRS DR1, and  $r$  mag. from SDSS DR16 (Chambers, et al. 2017; Ahumada et al. 2020).  $a$  is calculated as  $m_{\text{qui}} - m_{\text{max}}$ . We obtain  $M_{\text{qui}}$  when both  $m_{\text{qui}}$  and  $d$  are available. For the colors ( $g - r$ ,  $r - i$ , and  $i - z$ ), we source them from Pan-STARRS DR1, and in cases where no counterpart is found there, we turn to SDSS DR16. Any color values that fall outside the range of  $\pm 3\sigma$  compared to the original samples for each color are treated as outliers and as missing values in our training data set. Regarding cross-matching of the catalogs mentioned, we identify the counterpart of the VSX sources as the closest object within  $r_{\text{match}}$  in each catalog.

AAVSO VSX undergoes continuous updates. Our training data set was created in February 2023.

In Figure 1, we provide an example that illustrates the distribution of the training data set in the feature space, specifically through a scatter plot of  $M_{\text{max}}$  and  $r - i$ . The numbers of the training dataset, along with the proportion of missing data, are summarized in Table 2. Our data set comprises a total of 3686 samples. Notably, a substantial portion of the data table is missing, primarily due to the absence of observations during faint quiescent phases. This is particularly pronounced in the case of WZ Sge stars, which have low luminosity at quiescence, resulting in a high

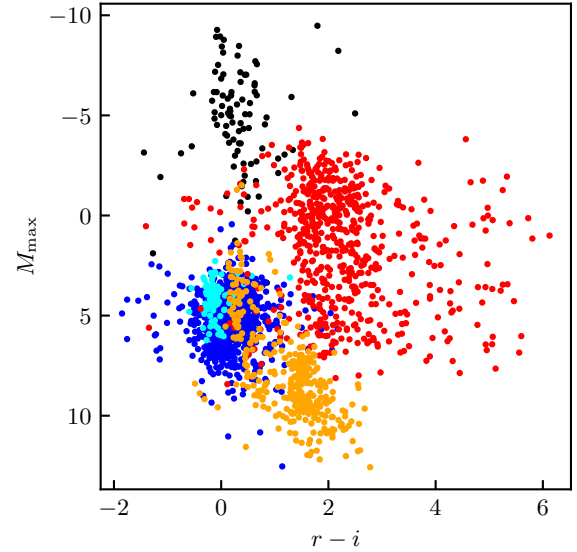


**Fig. 1.** Scatter plot of the training data set in  $M_{\text{max}}$  and  $r - i$ . The black, blue, cyan, red, and orange dots represent the samples of class N, DN, WZ, M, and F, respectively.

proportion of missing data. Novae, on the other hand, exhibit a relatively higher luminosity, but their significant distance from Earth results in faint quiescent apparent magnitudes, thus contributing to the high proportion of missing data.

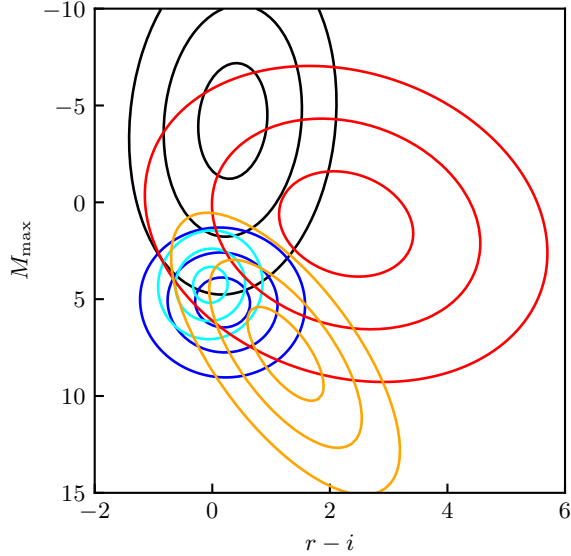
The distributions of the training data are approximated as normal distributions in equation (7), which give  $p(\mathbf{x}|k)$ . Their means and variance-covariance matrices are shown in Appendix 1. Figure 2 displays the marginal probability distribution of  $p(\mathbf{x}|k)$  corresponding to Figure 1, that is, within the  $M_{\text{max}}-(r - i)$  plane.

It should be noted that, in the classification of actual new transients, the available features vary from object to object. For example, if only three features,  $\ell$ ,  $b$ , and  $M_{\text{max}}$ , are available due to the absence of the quiescent counterpart, then  $\mu$  consists of these three elements and  $\Sigma$  contains a matrix of elements  $3 \times 3$ .

We evaluated the classifier's performance using leave-one-out cross-validation (LOOCV) with the training dataset (Hastie et al. 2017). The LOOCV accuracy was determined to be 0.813, and the confusion matrix is shown in Table 3. These results are based on all samples, including those with missing values for all features except ( $\ell, b$ ). There are 239 such samples, and they represent a challenge for accurate classification. When these samples are excluded, the classifier performance improves, achieving an accuracy of 0.869. Table 4 is the confusion matrix for this improved performance. This table shows a reduction in the number of misclassified samples compared to Table 3. In both cases, a substantial portion

**Table 2.** Training data set and fraction of the missing data.

Types of Var.	Class	N	$\ell$	$b$	$M_{\max}$	$M_{\text{qui}}$	$a$	$g-r$	$r-i$	$i-z$
Nova	N	332	0.00	0.00	0.53	0.53	0.13	0.50	0.49	0.46
Dwarf nova	DN	1528	0.00	0.00	0.30	0.30	0.05	0.23	0.23	0.25
WZ Sge-type DN	WZ	232	0.00	0.00	0.61	0.62	0.29	0.42	0.44	0.53
Mira	M	1062	0.00	0.00	0.14	0.14	0.00	0.32	0.32	0.34
Flare star	F	532	0.00	0.00	0.22	0.22	0.12	0.29	0.28	0.27

**Fig. 2.** Marginal probability distributions of  $p(\mathbf{x}|k)$  on the  $M_{\max}-(r-i)$  plane. The black, blue, cyan, red, and orange curves depict that of class N, DN, WZ, M, and F, respectively. For the observed distribution, see Figure 1.**Table 3.** Confusion matrix of the classifier for all samples in the training data set.

Pred. \ Label	N	DN	WZ	M	F
N	292	41	16	0	17
DN	13	1070	43	2	35
WZ	12	320	145	1	16
M	12	37	25	1048	22
F	3	60	3	11	442
Accuracy	0.880	0.700	0.625	0.987	0.831

of the DN samples is misclassified as WZ. This occurs because they occupy overlapping regions within the feature space. The information given by the eight features is not sufficient to classify them perfectly. It is essential to note that the primary objective of Smart Kanata is not to develop a high-performance classifier but rather to facilitate optimal follow-up observations. Consequently, the presence of classes that cannot be precisely separated is not significant.

## 2.4 Decision making of the follow-up observation mode

The follow-up observation modes  $B-V$ , EW, and Var are indexed as  $m = 1, 2$ , and  $3$ , respectively. As described in §2.2, we need  $q(y_m|k)$  to compute  $I_{\mathbf{x}}(K; Y_m)$  in addition to  $\pi(k)$  and  $p(\mathbf{x}|k)$ . We established  $q(y_m|k)$  based on observed data, as follows.

First, we examine the  $B-V$  distributions ( $m = 1$ ) for four

**Table 4.** Confusion matrix of the classifier for the samples which have more than three features.

Pred. \ Label	N	DN	WZ	M	F
N	264	18	3	0	9
DN	13	1050	19	2	33
WZ	7	310	144	0	0
M	12	17	0	1048	9
F	1	57	0	11	420
Accuracy	0.889	0.723	0.867	0.988	0.892

classes: N, DN, WZ, and M, drawing data from the AAVSO database. For the samples of our training dataset discussed in § 2.2, the  $B-V$  values at their maximum brightness were calculated using simultaneous observations in the  $B$  and  $V$  bands obtained from AAVSO. For classes N, DN, and WZ, the data at maximum was defined as observations made within a 2-day window from the observed peak. In the case of class M, this window was extended to 10 days because their variation time-scale is longer than the other classes. For class F, we used their quiescent color because flares typically have very short time-scales, and our follow-up observations are expected to capture their quiescent state following the flare. The  $B-V$  values for class F objects were derived from their  $g-r$  values in Pan-STARRS DR1, applying the transformation described in Tonry et al. (2012). As a result, we obtain the observed  $B-V$  distributions for all five classes, as shown in the left panel of Figure 3.

We approximate the observed distributions using two types of probability distributions to obtain  $q(y_m|k)$ . For apparently symmetric distributions, we employ normal distributions  $\mathcal{N}(\mu, \sigma)$ . On the other hand, for highly asymmetric distributions, we use Gumbel distributions  $\mathcal{G}(\mu, \beta)$  whose density function is defined as:

$$f(x) = \frac{1}{\beta} \exp \left\{ -\frac{x-\mu}{\beta} - \exp \left( -\frac{x-\mu}{\beta} \right) \right\} \quad (8)$$

In both cases, we estimate the parameters  $\mu$ ,  $\sigma$ , and  $\beta$  from the available samples. A summary of these  $q(y_m|k)$ , is shown in Table 5.

Second, we examine the distribution of H $\alpha$  EW ( $m = 2$ ) for the five classes. For classes N, DN, and WZ, we gathered EW data from Astronomer's Telegram (ATel)<sup>3</sup> and published papers. Specifically, for class N, we considered EW data observed within a 10-day window from the discovery. Most of the data for class N originated from ATel, while the data for classes DN and WZ primarily came from Tampo et al. (2021) and Han et al. (2020). The dataset sizes for classes N, DN, and WZ were relatively small, comprising 26, 28, and 15 samples, respectively. Given the absence of significant differences in the distributions between classes DN and WZ, we combined the data from these two classes. For class M, we calculated EW for 257 Mira-type objects, using the LAMOST database (Yao et al. 2017). For class F, we relied on

<sup>3</sup> <https://www.astronomerstelegram.org>

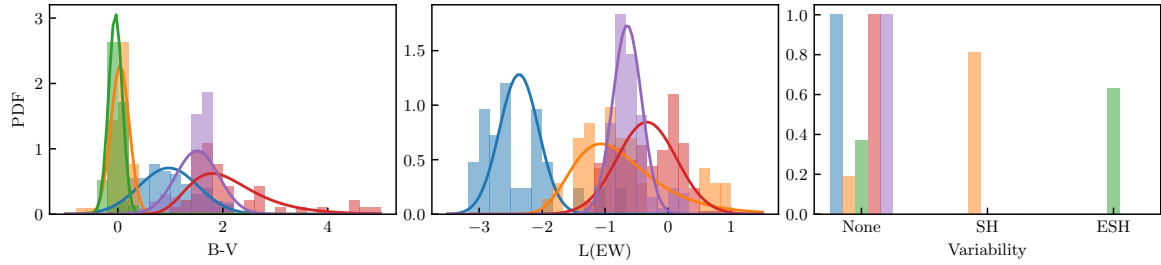


**Fig. 3.** Observed distributions of  $y_m$ , that is,  $B - V$  ( $m = 1$ , left), EW of  $H\alpha$  ( $m = 2$ , middle), and short-term variability ( $m = 3$ , right). The blue, orange, green, red, and purple curves depict the probability density functions for class N, DN, WZ, M, and F, respectively. In the middle panel, the orange histogram and curve represent the combined class of classes DN and WZ.

**Table 5.** List of  $q(y_m|k)$ , probability distributions of  $y_m$  for each class.

$m$	$k =$ Mode	1 N	2 DN	3 WZ	4 M	5 F
1	$B - V$	$\mathcal{N}(0.97, 0.56)$	$\mathcal{N}(0.04, 0.18)$	$\mathcal{N}(-0.05, 0.13)$	$\mathcal{G}(1.80, 0.59)$	$\mathcal{N}(1.51, 0.41)$
2	EW	$\mathcal{N}(-2.37, 0.31)$	$\mathcal{G}(-1.07, 0.57)$	$\mathcal{G}(-1.07, 0.57)$	$\mathcal{N}(-0.34, 0.47)$	$\mathcal{N}(-0.65, 0.23)$
3	Var*	[1.00, 0.00, 0.00]	[0.19, 0.81, 0.00]	[0.20, 0.00, 0.80]	[1.00, 0.00, 0.00]	[1.00, 0.00, 0.00]

\* The three elements represent the detection probabilities of [no periodic variation, ordinary superhumps, early superhumps].

351 EW measurements from quiescent UV Cet stars reported in Gershberg et al. (1999).

EW values are positive for the absorption lines and negative for the emission lines. In the case of class N, most EW values are below  $-100 \text{ \AA}$  and can even reach as low as  $-1000 \text{ \AA}$ , whereas for other classes, they mainly fall between  $-1 \text{ \AA}$  and  $0 \text{ \AA}$ . To effectively handle the distribution of EW that covers three orders of magnitude, we transform EW using the function:

$$L(\text{EW}) = \text{sgn}(\text{EW}_{H\alpha}) \log_{10}(1 + |\text{EW}_{H\alpha}|) \quad (9)$$

The histograms presented in the middle panel of Figure 3 illustrate the observed distributions of  $L(\text{EW})$ . We approximate these distributions using the normal and Gumbel distributions as detailed in Table 5, which are represented by the curves in the middle panel of Figure 3. It is important to note that for class N, we estimate the value of  $\sigma$  in the observed distribution of  $L(\text{EW})$  by excluding outliers with exceptionally large  $L(\text{EW})$ . This adjustment enables Smart Kanata to prioritize spectroscopic observations when both class N and either class WZ or DN have high class-probabilities.

Third, we employ discrete probability distributions for three types of short-term variations which are investigated by mode Var observations ( $m = 3$ ): No periodic variations ( $P_{\text{no}}$ ), ordinary superhumps ( $P_{\text{SH}}$ ), and early superhumps ( $P_{\text{ESH}}$ ). Ordinary superhumps are associated with SU UMa-type dwarf novae and exhibit periodic variations typically with a few percent longer period than the binary orbital period. In contrast, SS Cyg-type dwarf novae do not display superhumps. For class DN, we set  $P_{\text{no}}$ , representing the probability that a newly detected event is an outburst of SS Cyg objects, at 0.19, while  $P_{\text{SH}}$ , indicating the probability for SU UMa objects, is set to 0.81. These probabilities are based on the population of dwarf novae identified by SDSS (Inight et al. 2023). According to Kato (2015), the fraction of early superhumps detectable with an amplitude greater than 0.02 mag is 0.63. Therefore, we set  $P_{\text{ESH}} = 0.63$  and  $P_{\text{no}} = 0.27$  for class WZ. On the other hand, classes N, M, and F do not show any periodic variations like superhumps or early superhumps, so  $P_{\text{no}} = 1$  for them. The probability distributions, represented as  $[P_{\text{no}}, P_{\text{SH}}, P_{\text{ESH}}]$ , are summarized in Table 5. These distributions may include zero prob-

abilities, which we replace with small values ( $10^{-10}$ ) for calculations in equation (5).

## 2.5 Follow-up observation

We use two instruments for our follow-up observations: Hiroshima Optical and Near-Infrared camera (HONIR; Akitaya et al. 2014) and Hiroshima One-shot Wide-field Polarimeter (HOWPol; Kawabata et al. 2008). HONIR is mounted at the Cassegrain focus of Kanata. It has one CCD and one HgCdTe array, enabling us to simultaneously obtain optical and near-infrared images. We use it for the imaging observation in Smart Kanata, that is, mode  $B - V$  and Var. For events with a discovery magnitude of  $> 12.0$  mag, we set an exposure time of 60 s, while for brighter events, it is reduced to 30 s. We collect a set of  $B$  and  $V$  band images for mode  $B - V$ , while we obtain time-series  $V$  and  $J$  band images covering a four-hour duration for mode Var. A four-hour run covers 2–3 orbital periods of WZ Sge stars, thereby allowing us to identify the nature of short-term variations. HOWPol is attached to the Nasmyth focus and is used for spectroscopic observations. We obtain a low-resolution ( $R \sim 300$ ) spectrum with a wavelength coverage from  $4000 \text{ \AA}$  to  $8500 \text{ \AA}$  using HOWPol in mode EW. The exposure time for spectroscopy is set at 120 s.

Figure 4 shows the flowchart of the observation process. After receiving alerts from online platforms and selecting potential targets by excluding SNe and AGN activity as described in Section 2.1, Smart Kanata initiates follow-up observations. These observations fall into three scenarios.

In the first case, Smart Kanata triggers the observation when it detects transient events belonging to known novae or WZ Sge-type DN (§ 2.1). For novae, it initiates spectroscopic observations, whereas for WZ Sge-type objects, it initiates time-series imaging. In both modes, the observations will continue for 4 hours or until dawn. The second case involves triggering the observation when the object is classified as class N or WZ with a high probability:  $p(k|\mathbf{x}) > p_{\text{obs}}$ . The default value of  $p_{\text{obs}}$  is 0.95, as shown in Table 1. The observation modes follow the first case.

In the third case, Smart Kanata triggers the observation with the

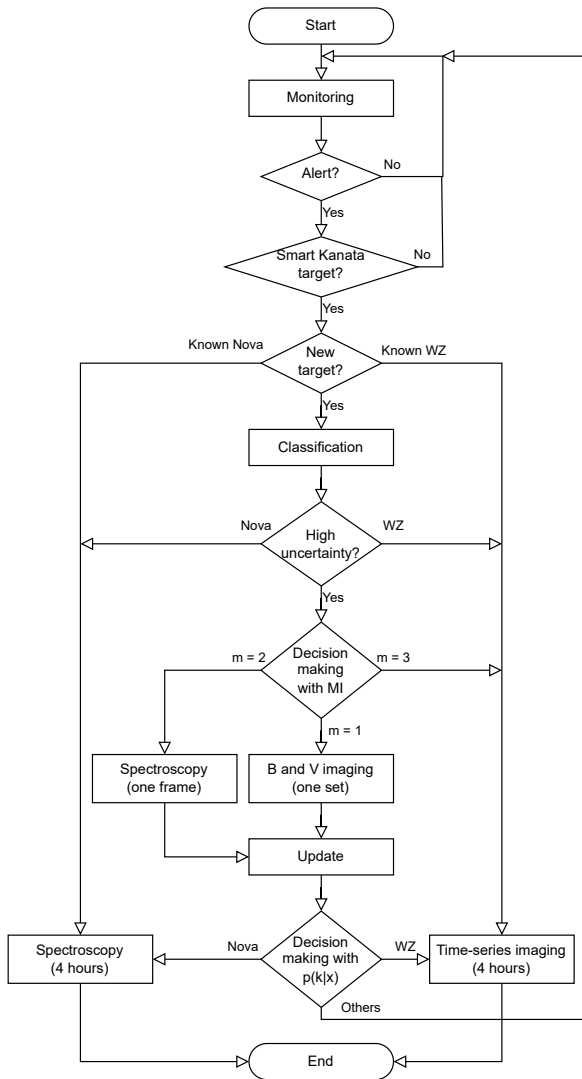


Fig. 4. Flowchart of the follow-up observation process in Smart Kanata.

highest  $I_{\mathbf{x}}(K; Y_m)$  mode when  $p_{\text{target}} = p(N|\mathbf{x}) + p(WZ|\mathbf{x}) > 0.1$ . In this case, after completing the initial follow-up observation process, we update the class probability and determine the next observation mode. We calculate the updated class probability using the observed value  $y_{m,\text{obs}}$  according to the formula:

$$p'(k|y_{m,\text{obs}}, \mathbf{x}) = \frac{q(y_{m,\text{obs}}|k)p(k|\mathbf{x})}{\sum_k q(y_{m,\text{obs}}|k)p(k|\mathbf{x})} \quad (10)$$

If class N has the highest  $p'$ , we perform time-series spectroscopic observations, while if class WZ has the highest probability, we perform time-series imaging. In other cases, the program returns to the main loop.

Before triggering any of the mentioned observation processes, we perform checks on conditions to confirm whether observation is feasible. These checks include the following parameters: time, position in the sky, telescope availability, and weather. The observable time is restricted to periods before and after civil twilight. The telescope has a hardware limitation, setting the lowest observable altitude to 10 degrees. Observations are only initiated when the telescope's server program is operational. To check weather conditions, we implemented a weather classifier using a convo-

lutional neural network (CNN), employing data from our all-sky camera located on the observatory roof. Additional details about this weather classifier are provided in the Appendix 2.

### 3 Results

#### 3.1 System evaluation

Smart Kanata was partially operational from 2021 to 2023 while under development. During this phase, only the time-series imaging mode, that is, mode Var, was available for follow-up observations. On 11 November 2022, the system successfully performed its first automated observation, targeting ZTF22abteqxm<sup>4</sup>. The object was confirmed to be a WZ Sge-type object ZTF22abteqxm<sup>5</sup>. The results of this observation will be detailed in a forthcoming paper (Sazaki, et al., in prep.).

Following the addition of multicolor imaging and spectroscopy modes, Smart Kanata entered full operational status on 18 December 2023. Table 6 lists the events that Smart Kanata attempted to initiate following-up observations during this phase, covering the period until October 2024. The table does not include targets observed during the partial operation phase mentioned above.

Out of the 21 opportunities for automated follow-up observations, the system completed two observations successfully. In three cases, the system stopped follow-up observations as the target probability,  $p_{\text{target}} < 0.1$ . The remaining 16 observation opportunities were missed due to poor weather (nine cases) or the observatory being closed (six cases) or system failure (one case).

In Table 6, the maximum values for class probabilities are highlighted in bold. The confusion matrix for the classifier is shown in Table 7. We defined the prediction of the classifier based on the class with the highest probability among the five possible classes to produce this confusion matrix. For two cases where the dwarf nova subclass was ambiguous, we assigned a value of 0.5 to the DN and WZ classes in Table 7. The classifier predictions matched the true classes in 11.5 cases, yielding an accuracy of 0.575. Among the 8.5 misclassified objects, three cases were objects that the classifier did not account for (two microlensing events and one GRB afterglow), and 5.5 cases had high uncertainties, with the highest probability in each case less than 0.5.

In three cases, MI was less than 0.001, indicating low class uncertainty. For the other 18 cases, MI was highest for mode  $B - V$  in five instances, mode EW in five, and mode Var in eight. The system tended to select the mode  $B - V$  when the uncertainty of the class was high, while mode EW was most likely chosen when there was a significant probability of the class N. Mode Var was typically selected when the probability of class N was lower. Overall, the selections of the follow-up mode were appropriate and there were no clearly incorrect decisions.

We successfully conducted automated observations of TCP J17395720–2627410 (V4370 Oph) and TCP J17440698–2125195. Details of these objects are discussed in the following subsection. Notes on other individual objects are provided below:

<sup>4</sup> TNS: <https://www.wis-tns.org/object/2022zxb>

<sup>5</sup> [vsnet-alert 27099] <http://ooruri.kusastro.kyoto-u.ac.jp/mailman3/hyperkitty/list/vsnet-alert@ooruri.kusastro.kyoto-u.ac.jp/message/NULUCDEKJRSR6CRVW5WMWRPUAOWJVVULU/>

**Table 6.** Class probability and MI for our targets.

Time (UT)	ID	Observer	Class probability	MI	Class	Status
			[N, DN, WZ, M, F]	[ $B - V$ , EW, Var.]		
23 Dec. 2023	ATLAS23xus	ATLAS	[0.000, 0.167, <b>0.833</b> , 0.000, 0.000]	[0.054, 0.000, <b>0.524</b> ]	WZ: <sup>1</sup>	(Bad weather)
29 Dec. 2023	Gaia23duw	Gaia Alert	[0.000, <b>0.994</b> , 0.006, 0.000, 0.000]	[0.002, 0.000, <b>0.044</b> ]	DN <sup>2</sup>	(Bad weather)
31 Dec. 2023	ATLAS23yai	ATLAS	[0.000, 0.256, <b>0.744</b> , 0.000, 0.000]	[0.072, 0.000, <b>0.662</b> ]	WZ:	(Closed)
17 Jan. 2024	TCP J03205377+4227578	XOSS	[0.000, 0.000, 0.000, 0.000, <b>1.000</b> ]	[0.000, 0.000, 0.000]	F <sup>3</sup>	( $p_{\text{target}} < 0.1$ )
23 Jan. 2024	TCP J07593036+0459025	Nakamura, Y.	[0.003, 0.027, <b>0.970</b> , 0.000, 0.000]	[0.037, 0.024, <b>0.151</b> ]	DN <sup>4</sup>	(Bad weather)
25 Jan. 2024	MASTER OT J174112.75+232535.1	MASTER	[0.011, 0.018, <b>0.971</b> , 0.000, 0.000]	[0.079, 0.070, <b>0.130</b> ]	WZ:	(Bad weather)
10 Mar. 2024	TCP J17395720-2627410/V4370 Oph	Kojima, T.	[ <b>0.997</b> , 0.000, 0.000, 0.000, 0.002]	[0.003, <b>0.027</b> , 0.000]	N	Success
19 Mar. 2024	ASASSN-24ca	ASAS-SN	[ <b>0.506</b> , 0.257, 0.189, 0.004, 0.045]	[0.778, 0.940, <b>0.978</b> ]	N <sup>5</sup>	(Closed)
26 Mar. 2024	TCP J18595064+0605336	Ueda, S.	[ <b>0.452</b> , 0.122, 0.092, 0.257, 0.078]	[0.903, <b>1.062</b> , 0.680]	F	(Closed)
12 May 2024	TCP J14231331-3658253	BraTS	[0.104, <b>0.273</b> , 0.248, 0.177, 0.198]	[ <b>1.119</b> , 0.666, 1.029]	DN:WZ:	(Bad Weather)
15 Jul. 2024	KATS24N014	XOSS	[0.229, 0.211, 0.164, <b>0.258</b> , 0.137]	[ <b>1.097</b> , 0.914, 0.916]	DN:WZ:	(Bad Weather)
15 Jul. 2024	KATS24N015	XOSS	[0.139, <b>0.265</b> , 0.223, 0.199, 0.174]	[ <b>1.122</b> , 0.748, 1.010]	WZ:	(Bad Weather)
20 Jul. 2024	TCP J17490276-2324066	Itagaki, K.	[ <b>0.996</b> , 0.003, 0.001, 0.000, 0.000]	[0.012, <b>0.031</b> , 0.030]	N <sup>6</sup>	(Closed)
22 Jul. 2024	TCP J18111965-2822416	Kojima, T.	[0.000, <b>1.000</b> , 0.000, 0.000, 0.000]	[0.000, 0.000, 0.000]	Microlensing <sup>7</sup>	( $p_{\text{target}} < 0.1$ )
11 Aug. 2024	TCP J17440698-2125195	Kojima, T.	[ <b>0.771</b> , 0.000, 0.000, 0.229, 0.000]	[0.342, <b>0.762</b> , 0.000]	Microlensing	Success
9 Sep. 2024	TCP J17064645-3528079	Itagaki, K.	[ <b>0.474</b> , 0.115, 0.090, 0.249, 0.073]	[0.881, <b>1.061</b> , 0.663]	N <sup>8</sup>	(Closed)
17 Sep. 2024	TCP J22481420+0629564	Nakamura, Y.	[0.000, 0.265, 0.338, 0.011, <b>0.386</b> ]	[1.015, 0.277, <b>1.050</b> ]	-	(Closed)
20 Sep. 2024	PSP24V	XOSS	[0.000, 0.000, 0.000, 0.000, <b>1.000</b> ]	[0.000, 0.000, 0.000]	F <sup>9</sup>	( $p_{\text{target}} < 0.1$ )
4 Oct. 2024	MASTER OT J065054.42+593625.5	MASTER	[0.003, 0.025, <b>0.972</b> , 0.000, 0.000]	[0.033, 0.020, <b>0.142</b> ]	WZ <sup>10,11</sup>	(Bad Weather)
21 Oct. 2024	TCP J20233423+1142122	Itagaki, K.	[ <b>0.291</b> , 0.178, 0.141, 0.260, 0.131]	[ <b>1.053</b> , 0.993, 0.849]	F <sup>12</sup>	Failure
29 Oct. 2024	MASTER OT J214120.16+050453.4	MASTER	[0.014, 0.299, 0.304, 0.073, <b>0.310</b> ]	[ <b>1.061</b> , 0.355, 1.055]	GRB <sup>13</sup>	(Bad weather)

<sup>1</sup> vstnet-alert 27977 <sup>2</sup> Hodgkin et al. (2023) <sup>3</sup> <http://xjltip.china-vo.org/psp24d.html> <sup>4</sup> vsnet-alert 27986 <sup>5</sup> Strader et al. (2024) <sup>6</sup> Munari et al. (2024b)<sup>7</sup> <http://www.cbat.eps.harvard.edu/unconf/followups/J18111965-2822416.html> <sup>8</sup> Tampo (2024) <sup>9</sup> <http://xjltip.china-vo.org/psp24v.html> <sup>10</sup> Killestein et al. (2024) <sup>11</sup> vsnet-alert 28024<sup>12</sup> <http://www.cbat.eps.harvard.edu/unconf/followups/J20233423+1142122.html> <sup>13</sup> <https://www.wis-tns.org/object/2024zse>



**Table 7.** Confusion matrix of the classifier for the real data set.

Label Pred.	Label					
	N	DN	WZ	M	F	Others
N	4	0	0	0	2	1
DN	0	1.5	1.5	0	0	1
WZ	0	1	4	0	0	0
M	0	0.5	0.5	0	0	0
F	0	0	0	0	2	1
Accuracy	1.000	0.500	0.667	—	0.500	—

**ATLAS23yai:** Zhao, Gao (2024a) identified this object as a dwarf nova based on optical spectra. ASAS-SN observations indicated a peak brightness of 14.3 mag, with an outburst duration of more than eight days, followed by rebrightening events after a temporary fade. The activity persisted for over 32 days from detection to the end of the rebrightening events. Its quiescent counterpart was found in the Pan-STARRS catalog with  $g = 21.85$ , suggesting an outburst amplitude of  $\sim 7.5$  mag. This large amplitude and prolonged activity suggest that the object is likely of class WZ rather than DN.

**MASTER OT J174112.75+232535.1:** ASAS-SN observations recorded the object showing an exponential decay at a rate of  $\sim 0.1 \text{ mag d}^{-1}$  over ten days. Following this, the object faded below the detection limit, consistent with a superoutburst of a dwarf nova. The discovery report<sup>6</sup> noted an outburst amplitude of 8.1 mag. Despite the absence of spectral data, the light curve and high amplitude strongly favor classification as a WZ-type object.

**TCP J18595064+0605336:** This flare star was misclassified by Smart Kanata. The system assigned the highest probability of 0.452 to class N, followed by 0.257 to class M, and a smaller probability of 0.078 to class F. This misclassification was caused by a large positional error in the discovery report. No quiescent counterpart was found within  $r_{\text{mat.ch}} = 2''.0$ , though a candidate YSO located  $2''.2$  from the reported position ( $g = 16.8$ ) was identified (Zari et al. 2018). Combined with ROSAT X-ray data, the object is classified as class F (Freund et al. 2022).

**TCP J14231331–3658253:** Discovered by Brazilian Transient Search (BraTS)<sup>7</sup> at 15.1 mag, this object exhibited a steady fading of  $\sim 0.2 \text{ mag d}^{-1}$  over six days, consistent with either class DN or WZ. No quiescent counterpart was found in available catalogs, implying a large outburst amplitude. However, due to the short focal length of the BraTS system (616 mm), there may be a significant positional error. A Gaia object with  $G = 18.4$  lies  $4''.3$  away, and if this is the quiescent counterpart, the outburst amplitude would be smaller,  $\sim 3$  mag. Thus, the subclass of this dwarf nova remains uncertain.

**KATS24N014:** A spectrum reported by Zhao, Gao (2024b) showed a blue continuum with a narrow H $\alpha$  emission line, suggesting the object belongs to class DN or WZ. ASAS-SN observations confirmed an outburst lasting at least five days. The absence of a quiescent counterpart implies a large outburst amplitude, but the precise subclass remains unclear.

**KATS24N015:** Zhao, Gao (2024b) report a spectrum showing a blue continuum with Balmer absorption lines, indicating that the object likely belongs to class DN or WZ. The ASAS-SN light curve reveals a main outburst lasting more than 12 days, followed by a temporary fading and subsequent rebrightenings. The object's active phase has persisted for over 40 days. Its quiescent counterpart, with  $b = 21.43$ , was identified in the APM-North

**Table 8.** Observation log of V4370 Oph.

MJD*	$T_{\text{exp}}^{\dagger}$ (s)	$\Delta t^{\ddagger}$ (d)	$R^{\S}$
60379.84682	120	0.06282	260
60379.84843	120	0.06443	300
60379.85004	120	0.06604	300
60379.85362	120	0.06962	300
60379.85522	120	0.07122	300
60379.85682	120	0.07282	300
60384.84319	200	5.05919	230
60384.84688	200	5.06288	190
60384.85036	200	5.06636	200

\*Time of the exposure center.  $\dagger$ Exposure time.

$\ddagger$ Time since the discovery (2024 March 10.784

UT)  $\S$ Spectral resolution:  $\lambda/\Delta\lambda$

Catalogue (McMahon et al. 2000), suggesting an outburst amplitude of  $\gtrsim 7$  mag. The extended activity and large amplitude strongly support the classification of the object as a member of class WZ.

**TCP J20233423+1142122:** Discovered by Itagaki at 10.2 mag, this object exhibited a rapid decline to 13.2 mag within 25 min.<sup>8</sup>. Smart Kanata did not identify a quiescent counterpart, assigning the highest probability of 0.291 to class N. Although the system tried to initiate an automated observation in mode  $B - V$ , the observation was canceled due to a network connection error. A significant positional discrepancy exists in the discovery report, with a Gaia DR3 source of  $G = 14.08$  located  $3''.59$  from the reported position. Based on this and ROSAT X-ray data, the object is classified as class F.

## 3.2 Initial results

### 3.2.1 Classical nova: V4370 Oph

A new object with 11.5 mag was discovered by T. Kojima in an image taken on 10.784 (UT) March 2024 and was promptly reported to TOCP. It was designated as TCP J17395720–2627410. No object brighter than 15 mag was detected at the corresponding position in an image taken on 9.81 (UT) March 2024 by M. Yamamoto.<sup>9</sup> This discovery report was detected by Smart Kanata, which classified the object as a nova with a probability of 0.997 and initiated spectroscopic observations using HOWPol automatically. A preliminary analysis of the collected data revealed broad Balmer and He I emission lines exhibiting P-Cygni profiles, thus confirming its nova classification (Uemura, Nakaoka 2024). Subsequent to this spectroscopic observation, the object was assigned the GCVS name V4370 Oph (Kazarovets 2024).

Our observation log for V4370 Oph is presented in Table 8. The initial exposure started 1.49 hours after discovery. Observations persisted for 16.4 min, yielding six frames. After bias subtraction and flat-field correction, one-dimensional spectra were extracted from the images. Wavelength calibration was performed using the night-sky lines. Flux calibration was omitted because spectrophotometric standard stars were not observed. In the present study, we exclusively examine spectra normalized to the continuum flux level.

Figure 5 shows the spectra from the first day of observation. The mean normalized spectrum of the six spectra is represented by the black line, while the gray lines illustrate each individual spectrum to visualize variances around the mean. Panel (a) presents the

<sup>6</sup> <https://www.wis-tns.org/object/2024aud>

<sup>7</sup> [http://sites.mpc.com.br/holvorcem/obs/SkySift\\_disc\\_transients.html](http://sites.mpc.com.br/holvorcem/obs/SkySift_disc_transients.html)

<sup>8</sup> <http://www.cbat.eps.harvard.edu/unconf/followups/J20233423+1142122.html>

<sup>9</sup> <http://www.cbat.eps.harvard.edu/unconf/followups/J17395720-2627410.html>

spectra throughout the wavelength range, where the Balmer and He I emission lines exhibit prominent P-Cygni profiles. The EW, the full width at half maximum (FWHM), and the velocity of the minimum of the absorption component ( $v_{\text{abs}}$ ) were measured and summarized in Table 9. These measurements were conducted for each of the six spectra, with the table listing the means and standard deviations of these measurements. The EWs are relatively small, approximately  $\sim 20 \text{ \AA}$ , even for  $H\alpha$ . This observation, coupled with the pronounced P-Cygni profiles, suggests that the object was in the early stages of a nova eruption.

Panels (b) and (c) provide enlarged views of panel (a). In panel (b), a pronounced Na D absorption line is evident. The emission component of He I 5876 likely overlaps with this absorption line. Furthermore, an absorption feature around  $5650 \text{ \AA}$  is noteworthy, likely representing a part of a P-Cygni profile, with its emission component observable in the range  $5670\text{--}5770 \text{ \AA}$ . This line is tentatively identified as N II 5679, although the width of the emission component exceeds what can only be attributed to this line. This excess indicates the contributions of Al III 5697 and 5723 to this broad emission component.

In panel (c), the P-Cygni profiles of  $H\beta$  and N II 5001 + He I 5016 are clearly observed. However, on the bluer side, no lines are clearly discernible due to substantial interstellar extinction, with  $A_V = 4.37$  along the line of sight to this object (Schlafly, Finkbeiner 2011). Nevertheless, indications of  $H\gamma$  and He I 4471 are visible, potentially exhibiting P-Cygni profiles. Another notable feature is a potential bump in the wavelength range  $4640\text{--}4720 \text{ \AA}$ . This bump is consistently observed not only in the mean spectrum, but also in each individual spectrum, supporting its validity. This wavelength region encompasses a band rich in high-excitation lines, known as the Bowen blend. However, the lack of a strong emission line of He II 4686 suggests that lower excitation lines contribute to the emission component. The bump is possibly identified as N II 4643, while N II 4630 is absent. Other candidates include moderately excited lines such as N III 4640 or C III 4650. The contribution of He I 4713 is also plausible.

We analyze short-term variations of the emission lines in our six spectra collected over a span of 14 min. using a Student  $t$  test. Let  $f_{ij}$  ( $i = 1, 2, \dots, 1099, j = 1, 2, \dots, 6$ ) represent the normalized flux at the  $i$ -th wavelength of the  $j$ -th spectrum. We modeled temporal variations at each wavelength as follows:

$$f_{ij} = a_i t_j + b_i + \varepsilon_i \quad (11)$$

$$\varepsilon_i \sim \mathcal{N}(0, \sigma_i^2), \quad (12)$$

where  $t_j$  denotes the time of the  $j$ -th spectrum, and  $\varepsilon_i$  represents Gaussian noise with a variance  $\sigma_i^2$ . We estimated  $a_i$ ,  $b_i$ , and  $\sigma_i^2$  using linear regression for each wavelength and tested  $a_i \neq 0$  using the Student  $t$  distribution.

Figure 6 illustrates the  $p$ -values for each wavelength. We can reject the null hypothesis of  $a = 0$ , indicating that  $f_i$  has no significant variation, with greater confidence at lower  $p$ -values. The dashed horizontal line represents a significance level of 0.01. The wavelengths that fall sporadically below  $p = 0.01$  can be considered false positives. However, a distinct band is observable containing multiple consecutive wavelengths with  $p < 0.01$  centered around  $H\alpha$ . This indicates that a significant variation is present in this wavelength band.

Figure 7 shows the  $p$ -values (top) and spectra (middle) centered on  $H\alpha$ . Small  $p$ -values are notably associated with the absorption component and the blue side of the emission component. To emphasize potential variations, we present the ratio of each spectrum to the mean spectrum in the bottom panel. Consistent with the  $p$ -values, significant deviations from the mean are observed across

the spectra, particularly from the absorption to the blue side of the emission components. This suggests a rapid deepening of the absorption component during our observation period.

In addition to the initial observation, we acquired three spectra on 15 March, five days after the discovery. The mean spectrum is depicted in Figure 8 (black line), with the mean spectrum from the first day serving as a reference (gray line). The spectrum exhibits typical characteristics for He/N novae after maximum: prominent Balmer, He I, and N II emission lines without any signs of high-excitation lines. The emission lines display a box-like profile with a more pronounced red peak. As detailed in Table 9, the object underwent a significant increase in both EW and FWHM of the lines from the first to the fifth day. These variations in line features suggest that the high-velocity components grew between the first and fifth days.

### 3.2.2 Microlensing event: TCP J17440698–2125195

TCP J17440698–2125195 was discovered by T. Kojima at 13.7 mag. on 11.4556 (UT) August 2024.<sup>10</sup> Smart Kanata found this discovery from the TOCP report, estimated class probabilities of 0.771 for class N and 0.229 for class M, made the decision to conduct follow-up observations in mode EW, and started spectroscopic observation on 11.53699 (UT) (MJD 60533.53699),  $\sim 1.9$  hours after the initial discovery. The spectrum is shown in Figure 9. It revealed no prominent emission lines, with  $H\alpha$  marginally detected in absorption. The EW of  $H\alpha$  was measured at  $\sim 4 \text{ \AA}$ , prompting the system to update the class probabilities to 0.000 for class N and 1.000 for class M. Consequently, the system classified the object as a Mira and discontinued follow-up observations.

The spectrum shown in Figure 9 is characterized by strong absorption lines of Na D and Mg I. The presence of the Na D line is consistent with a significant interstellar extinction in the direction of the object ( $A_V \sim 2$ ; Schlafly, Finkbeiner 2011). Along with the weak  $H\alpha$  absorption line, the Mg I absorption indicates a K-type star. Munari et al. (2024a) reported spectra taken on 12.863 (UT), 1.3 days after our observation, when the object had faded by  $\sim 1.3$  mag. Their spectrum shared common features with ours, and they suggested a spectral type of K2 to K3 and a luminosity class of III to II, consistent with the quiescent counterpart, which is likely a K-type giant, inferred from  $V = 16.80$  and  $B - V = 1.7$  ( $E(B - V) \sim 0.7$ ; Zacharias et al. 2004).

We conducted a follow-up imaging observation and obtained  $V = 16.46 \pm 0.17$  on 20.52148 August (MJD 60542.52148). Photometry was performed using a comparison star located at RA=17:44:05.15, Dec=  $-21:24:42.8$ , with  $V = 14.90$  in the NOMAD catalog (Zacharias et al. 2004). The light curve of TCP J17440698–2125195 is shown in Figure 10. ATLAS and the Gaia satellite detected a brightening of the object on 5 and 6 August, respectively. The event was designated as Gaia24cfb.<sup>11</sup> These data indicate that the object had already been active six days before T. Kojima's discovery. The timescale of variation near the maximum is short:  $\gtrsim 0.8$  mag in 1.0 days for the rise and 1.3 mag in 1.0 days for the decay. Our observation suggests that the object had nearly reached or was still slightly brighter than its quiescent level nine days after its peak brightness.

Although Smart Kanata initially classified the object as a Mira, the rapid rise and decline around the maximum are inconsistent

<sup>10</sup><http://www.cbat.eps.harvard.edu/unconf/followups/J17440698-2125195.html>

<sup>11</sup><http://gsaweb.ast.cam.ac.uk/alerts/alert/Gaia24cfb/>



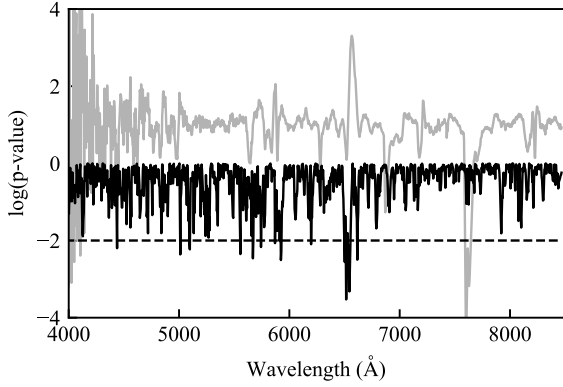


**Fig. 6.**  $p$ -values for each wavelength (black line). For details about the statistical test, refer to the main text. The gray line represents the mean spectrum shown in Figure 5. The dashed horizontal line represents  $p = 0.01$ .

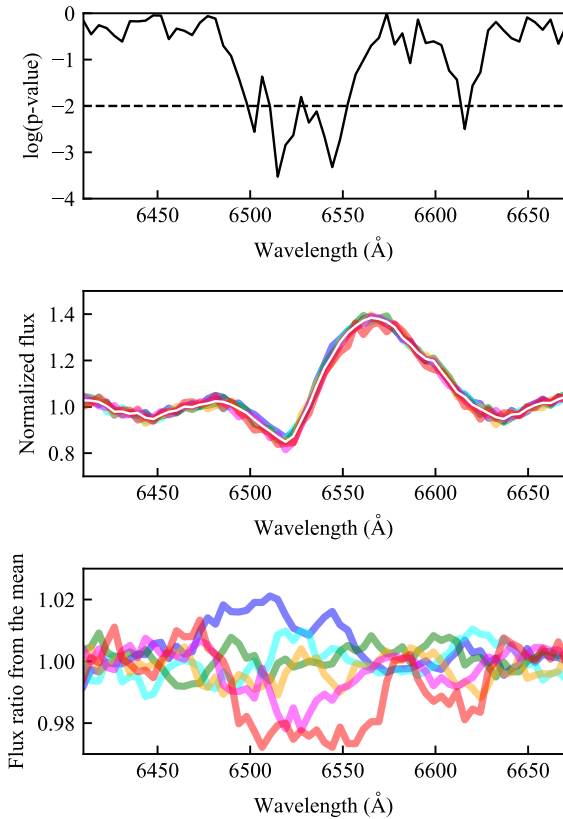


**Fig. 7.** Top:  $p$ -values around  $H\alpha$ . Middle: Spectra around  $H\alpha$ . The colored lines represent the six spectra. Colors progress from early (blue) to late (red), with intermediate colors including cyan, green, yellow, and magenta. The white line indicates their mean. Bottom: the ratio of each spectrum to the mean. To enhance clarity, we display 5-point running mean spectra in this panel.

**Table 10.** Confusion matrix of the LR classifier.

Pred. \ Label	Label				
	N	DN	WZ	M	F
N	248	25	10	11	15
DN	10	1050	10	2	32
WZ	26	252	146	0	1
M	5	2	0	1026	10
F	8	123	0	22	413
Accuracy	0.835	0.723	0.880	0.967	0.877

with this classification. In addition to the lack of significant spectral changes, the gradual rise and decay over approximately 10 days, combined with the rapid variation around the peak, suggest that this is actually a microlensing event.

Although microlensing events are not included in the list of variable star classes in Smart Kanata, the spectrum obtained by our system played a critical role in identifying its nature. This case demonstrates that Smart Kanata has the potential for serendipitous discoveries, even for unexpected and rare phenomena.

## 4 Discussion

As demonstrated in the previous section, Smart Kanata effectively supports decision making about follow-up observations of CVs. However, the GM classifier employed in Smart Kanata provides only a simple, quadratic decision boundary, despite the availability of alternative models that can offer nonlinear decision boundaries. In Section 4.1, we will compare the performance of other classification models with the GM classifier. Following this, Section 4.2 will focus on the implications of our observations of V4370 Oph.

### 4.1 Comparison with the performance of the other classification models

Logistic regression (LR) provides a linear classification model. The probability of multinomial LR is expressed as:

$$p(\mathbf{y}|\mathbf{x}, \mathbf{w}) = \frac{\exp(-\mathbf{w}_k^T \mathbf{x})}{\sum_j \exp(-\mathbf{w}_j^T \mathbf{x})}, \quad (13)$$

where  $\mathbf{w}_k$  is the coefficients to be optimized for class  $k$ , which include the bias factor. The objective variable is a "1-of- $K$ " encoding vector,  $\mathbf{y} = (y_1, y_2, \dots, y_K)$  such that  $y_k = 1$  if the sample belongs to the class  $k$ , and  $y_i = 0$  otherwise. The likelihood and log-likelihood functions are given as:

$$\ell(\mathbf{w}) = \prod_i \prod_k \left\{ \frac{\exp(-\mathbf{w}_k^T \mathbf{x}_i)}{\sum_j \exp(-\mathbf{w}_j^T \mathbf{x}_i)} \right\}^{y_{ik}} \quad (14)$$

$$\log \ell(\mathbf{w}) = \sum_i \sum_k y_{ik} \log \frac{\exp(-\mathbf{w}_k^T \mathbf{x}_i)}{\sum_j \exp(-\mathbf{w}_j^T \mathbf{x}_i)} \quad (15)$$

A nonlinear LR classifier can be obtained with the kernel method. In equation (13), the feature vector of the  $i$ -th sample  $\mathbf{x}_i$  can be replaced by  $\mathbf{x}'_i = (k(\mathbf{x}_0, \mathbf{x}_i), k(\mathbf{x}_1, \mathbf{x}_i), \dots, k(\mathbf{x}_N, \mathbf{x}_i))$ , where  $k(\cdot)$  is the kernel function. We use the RBF kernel:  $k(\mathbf{x}_i, \mathbf{x}_j) = \exp(-\|\mathbf{x}_i - \mathbf{x}_j\|_2^2 / 2\sigma^2)$ . The dimension of the new vector of features  $\mathbf{x}'$  increases from the number of features  $M$  to the number of samples  $N$ . To avoid overfitting,  $\ell_1$  regularization for  $\mathbf{w}$  is useful. The objective function is then  $E(\mathbf{w}) = \log \ell(\mathbf{w}) + \lambda \|\mathbf{w}\|_1$ . The model that optimizes  $E(\mathbf{w})$  is called the sparse multinomial logistic regression (SMLR).

We developed the LR and SMLR classifiers using samples that

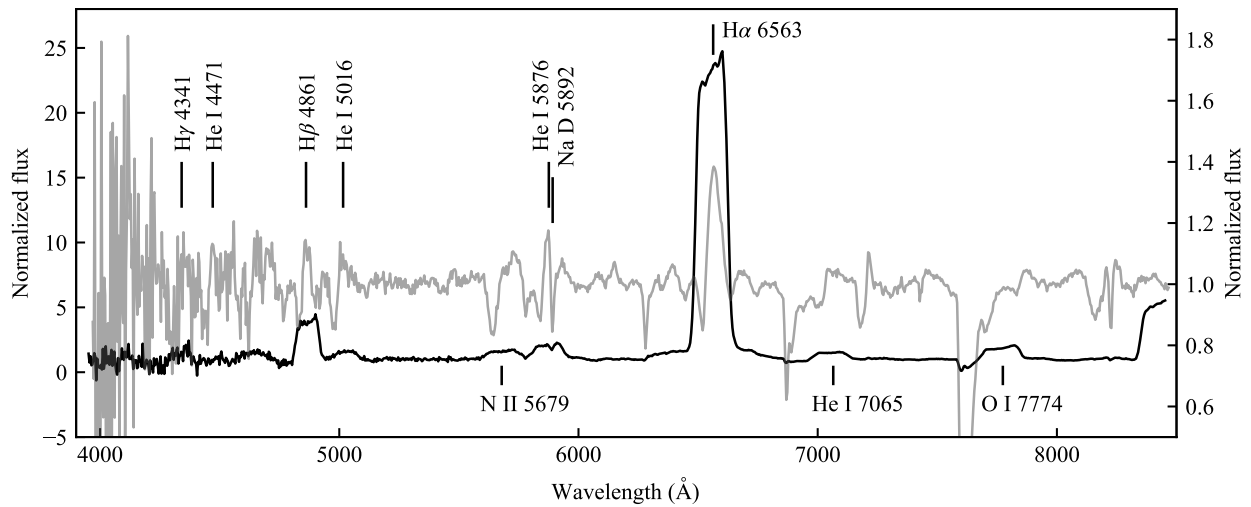


**Fig. 8.** Spectrum of V4370 Oph on March 15, five days after the discovery (black line). The spectrum on March 10 is depicted by the gray line.

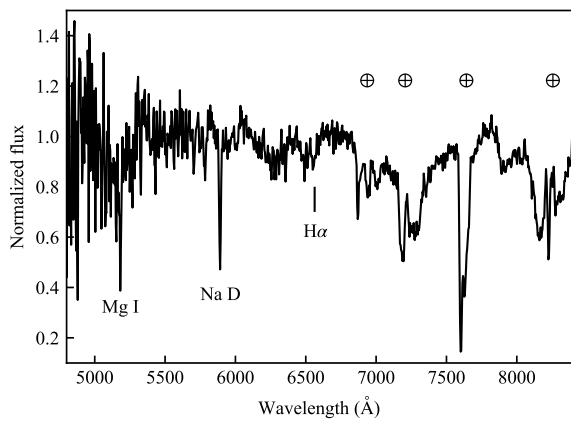


**Fig. 9.** Spectrum of TCP J17440698–2125195 on August 11.

**Table 11.** Confusion matrix of the SMLR classifier.

Pred. \ Label	N	DN	WZ	M	F
N	241	20	11	9	12
DN	14	1096	15	1	19
WZ	28	235	140	0	5
M	6	2	0	1030	6
F	8	99	0	21	429
Accuracy	0.811	0.755	0.843	0.971	0.911

have more than three features. Using the same samples, GM gives the confusion matrix in Table 4. The hyperparameters of SMLR,  $\lambda$  and  $\sigma^2$  were determined by 10-fold cross-validation. As a result, the cross-validated accuracies are 0.836, 0.852, and 0.869 for the optimized LR, SMLR and GM classifiers, respectively. Tables 10 and 11 are the confusion matrices for the LR and SMLR classifiers, respectively. The accuracy for SMLR and GM are comparable, and slightly higher than LR. There is no major difference in the characteristics of the confusion matrix for those three models: for example, all of them misclassify a significant part of DN as WZ.

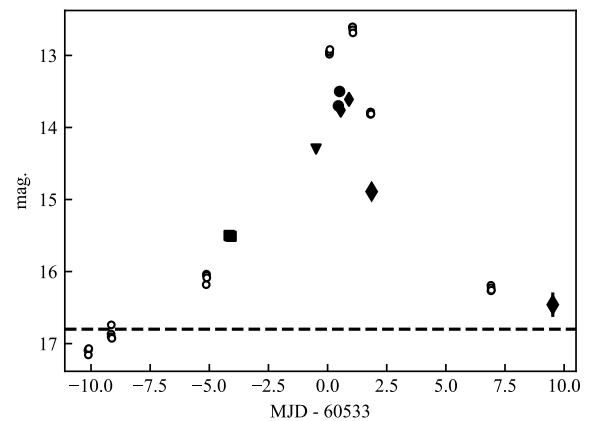


**Fig. 10.** Light curve of TCP J17440698–2125195. The filled squares, triangle, circles, and filled diamonds represents  $G$ -mag observed by Gaia, visual upper-limit reported in TOCP,  $V$ -band magnitudes in TOCP and (Munari et al. 2024a), and our observation, respectively. The open circles represents the ‘orange’ band magnitudes observed with ATLAS (Tonry et al. 2018; Smith et al. 2020). The dashed line indicates the quiescent level.

These results suggest that there is no significant difference in the performance of LR, SMLR, and GM.

LR and SMLR require training data sets without missing values to classify the target. As a result, they can use limited samples in the training data. On the other hand, GM can be developed using all values in the training data, which is an advantage for GM.

However, there are aspects of our classifier that warrant future improvement. Some of the missing values, such as distance and quiescent magnitude, are actually informative upper or lower limits. Additionally, the features  $M_{\max}$  and  $a$  should be treated as lower limits because they are derived from the magnitude at the time of discovery, when the object may still be in a rapid brightening phase. Implementing nonlinear classification models that can use them effectively will be an important direction for future

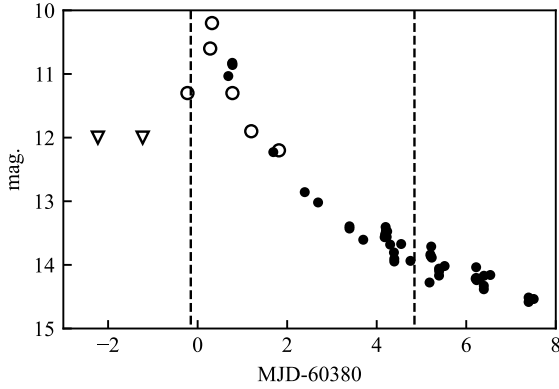


**Fig. 11.** Light curve of V4370 Oph. The data is from AAVSO. The open and filled circles denote visual and  $V$ -band magnitudes, respectively. The open triangles are upper-limits in the visual magnitude. The vertical dashed lines show the times of our spectroscopic observations.

research.

## 4.2 Mass ejection process in novae

V4370 Oph rapidly faded after reaching its optical maximum. Figure 11 illustrates the light curve of the object, sourced from AAVSO<sup>12</sup>. We removed systematic outliers of  $V$ -mag reported by specific observers. Assuming the observed maximum of 10.4 mag at MJD= 60380.3, we estimate the times for the object to decay by 2 and 3 mag from maximum light to be  $t_2 \sim 1.6$  d and  $t_3 \sim 3.0$  d, respectively. Consequently, V4370 Oph qualifies as a very fast nova. The maximum magnitude rate of decline (MMRD) relationship indicates that the object exhibits high luminosity at maximum and a high white dwarf mass (Livio 1992). Using the MMRD relation from Della Valle, Izzo (2020), the absolute magnitude in  $V$ -band,  $M_V$ , can be estimated as  $M_V = -7.78 - 0.81 \times \arctan((1.32 - \log(t_2))/0.23)$ , we obtain  $M_V = -8.9$  for  $t_2 = 1.6$  d. Distance to the object can be estimated as 9.6 kpc using the maximum magnitude observed of 10.4 mag and  $A_V = 4.37$  (Schlafly, Finkbeiner 2011). A quiescent counterpart with  $g = 21.71$  in the Pan-STARRS DR1 catalogue (Chambers, et al. 2017) suggests an absolute magnitude at quiescence of  $M_q = 6.8$ . This suggests a secondary star, likely a K-type main-sequence star or later, though this inference has significant uncertainty due to the large error in the distance estimation.

The times of our spectroscopic observations are indicated in Figure 11: the first observation occurred about 11 hours before the light curve maximum, while the second was during the decline phase. The spectra depicted in Figures 5 and 8 exhibit typical features of very fast novae, namely, P-Cygni profiles just before the maximum and broad emission lines after the maximum.

Owing to recent rapid discoveries, reports, and follow-up observations, the evolution of emission lines during the initial rising stage now provides new insights into the formation process of mass ejection in novae. Arai et al. (2015) identified highly excited lines of N V, IV, III, C IV, III, and He II during the rising phase of the recurrent nova T Pyx. They called this stage the Wolf-Rayet (WR) stage due to its spectral similarity. Aydi et al. (2023) report a comparable spectrum during the rising stage of the very slow

nova Gaia22alz. Additionally, Taguchi et al. (2023) successfully obtained spectra during the rising stage of V1405 Cas, revealing N III and He II lines, although lacking N V, IV, and C IV lines. These high-excitation lines exhibit no P Cygni profiles and have moderate velocities ( $1000\text{--}2000\text{ km s}^{-1}$ ).

The spectra of V4370 Oph on the first day showed indications of moderately excited lines of Al III, but lacked higher excitation lines, suggesting a lower excitation temperature compared to the aforementioned samples. The lack of highly excited lines and presence of Al III lines resemble the spectrum of V1405 Cas taken after the initial rapid rise and in the early stage of the pre-maximum halt (at 53.53 hours after its discovery) (Taguchi et al. 2023).

According to the standard model of nova eruptions (e.g., Bode, Evans 2008), the envelope surrounding a white dwarf begins to expand when the photospheric luminosity reaches the Eddington limit. This is the so-called fireball stage, during which a soft X-ray flash was recently detected in YZ Ret (König et al. 2022; Kato et al. 2022). Initially, the photospheric temperature is expected to be  $\lesssim 10^6$  K, decreasing gradually while maintaining a constant luminosity. The physical conditions likely resemble those of WR stars, with a photospheric temperature in the range of a few  $10^5$  K shortly after the onset of expansion. The high-excitation lines observed in T Pyx and Gaia22alz would likely originate under such conditions. In this scenario, our observation of V4370 Oph is definitely capturing a subsequent stage when the temperature decreases moderately, but still before reaching the minimum.

The decrease in photospheric temperature can also account for the rapid deepening of the absorption component of  $H\alpha$ , as shown in Figure 7. The variation in line profile was predominantly observed in the absorption component rather than the entire profile of the emission line. Therefore, it is likely attributed to changes not in the region where emission line photons are generated, but rather in the photosphere. Balmer absorption lines are expected to be weak in the condition that high-excitation lines are formed and hydrogen gas is fully ionized during the early WR stage. We propose that the reduction in photospheric temperature toward  $\sim 10^4$  K would consequently lead to the strengthening of the absorption component.

Yamanaka et al. (2010) also successfully obtained the time-series spectra of U Sco during its initial rising stage. Although the spectra exhibited no high- excited lines, rapid evolution of the high-velocity component was observed. The Balmer and He I emission lines showed a triple-peak profile, with the blue and red peaks at  $\sim 3000\text{ km s}^{-1}$  developing more rapidly than the central peak within 1.7 hours. These high- velocity components became dominant, and the emission lines exhibited a box- like profile one day after the initial observation. Furthermore, Aydi et al. (2020) reported early spectra of 12 novae and noted that the delayed growth of the high-velocity component is a common feature among novae.

The delayed appearance of the high-velocity component in emission lines implies a postponed launch of the optically thick wind (Kato, Hachisu 1994). This wind, expected to be formed due to acceleration by the iron opacity bump at  $\sim 1.5 \times 10^5$  K in the optically thick envelope, is proposed to experience a delay in its evolution due to binary interaction (Shen, Quataert 2022). According to Shen, Quataert (2022), a slow equatorial outflow is first driven by the binary interaction, and then the fast wind is launched after the acceleration region recedes within the WD Roche radius.

Our observations revealed no indication of a high-velocity component in the spectra of V4370 Oph on the first day, whereas a box-like profile was observed on the fifth day. Combined with the short  $t_2$  and  $t_3$  values, V4370 Oph potentially resembles U Sco, which also exhibited a box-like profile on the second day. The

<sup>12</sup><https://www.aavso.org>

stage at which we observed V4370 Oph on the first day may correspond to just before the stage observed in U Sco. In summary, we propose that the spectra of V4370 Oph taken on the first day correspond to the termination of the WR stage, during which the envelope's photosphere expands and the optically thick wind has yet to be launched.

However, the FWHM of the emission lines was already moderately high, exceeding  $1000 \text{ km s}^{-1}$ , on the first day. Furthermore, T Pyx and V1405 Cas also exhibited high velocities that exceeded  $1000 \text{ km s}^{-1}$  during the initial rising stage (Arai et al. 2015; Taguchi et al. 2023). If the optically thick wind had not yet formed, that is, the acceleration at the iron opacity bump had not been effective, another acceleration mechanism may be necessary to explain the initial outflow. The decay energy of  $\beta$ -unstable nuclei (mainly  $^{13}\text{N}$  and  $^{15}\text{O}$ ) can directly accelerate the envelope, although this would likely occur only in the very early phase when the polluted area is close to the envelope surface (Starrfield et al. 2016; Shen, Quataert 2022).

The scenario described above requires validation through further data, as previous samples display significant diversity in their light curves. Both V4370 Oph and U Sco are classified as very fast novae undergoing rapid rises. V1405 Cas also experienced a rapid rise; however, the object displayed a prolonged plateau with short-lived flares over 200 d (Taguchi et al. 2023). On the contrary, T Pyx first exhibited a rapid rise, followed by a gradual rise, and finally a slow decline (Chomiuk et al. 2014b). Gaia22alz is characterized as a very slow nova, with high excitation lines observed 49 days after the eruption onset, still during the initial rising stage (Aydi et al. 2023). It is not evident that the evolution of the emission lines is identical, as only the rising and decline time-scales differ. Additionally, geometric effects may play an important role in determining the velocity and profile variations, as novae have shown signs of aspherical ejecta (e.g., Chomiuk et al. 2014a). Therefore, more data covering a wide range of binary parameters are necessary to establish the observational features of the initial rising stage. We have demonstrated that Smart Kanata effectively contributes to this study through a case study of V4370 Oph.

## 5 Summary

We have developed Smart Kanata, an autonomous decision-making system for prompt follow-up observations of CVs using the 1.5-m Kanata telescope. The system selects the optimal observation mode with the highest MI among three possible options. This MI is calculated based on the class probabilities estimated from the GM classifier of variable star types and the likelihood functions constructed from known samples. During its  $\sim 300$  days of operation, our system demonstrated its capability to make appropriate decisions for follow-up observations across 21 samples. It successfully conducted automated spectroscopic observations for the nova V4370 Oph and the microlensing event TCP J17440698–2125195. Notably, in the time-series spectra of V4370 Oph, we observed a rapid deepening of the absorption component of the  $\text{H}\alpha$  line. These findings highlight the potential of Smart Kanata as a valuable tool for investigating the early phases of transient events in CVs.

Future developments for Smart Kanata include expanding the number of online platforms it monitors. These may include existing platforms such as Gaia Alerts (Hodgkin et al. 2021) and, in the future, transient events discovered by LSST (Ivezić et al. 2019). Additionally, updating the classification model to effectively han-

dle missing values in training data, as well as upper and lower limits, will be a critical improvement.

## Acknowledgments

We acknowledge with thanks the variable star observations from the AAVSO International Database contributed by observers worldwide and used in this research. We would like to thank the transient survey projects ATLAS, Gaia Alert, XOSS, MASTER, ASAS-SN, BraTS, as well as the databases TNS and CBAT, for providing prompt information about transients, which was essential in conducting this study.

## Funding

This work was supported by a Kakenhi Grant-in-Aid (No. 21K03616) from Japan Society for the Promotion of Science (JSPS).

## Appendix 1 Multivariate normal distributions of training samples for the GM classifier

As discussed in Section 2.3, we calculated the means and covariances of the training samples to construct a GM classifier. Table 12 lists the means, while Tables 13, 14, 15, 16, and 17 present the variance-covariance matrices for classes N, DN, WZ, M, and F, respectively. We note that class M has a negative mean for  $a$ , even though it is expected to be positive. This discrepancy arises because, as mentioned in Section 2.3,  $M_{\text{max}}$  is derived from relatively blue bands ( $V$ ,  $CV$ ,  $g$ , and  $pg$ ) in the VSX catalog, while  $M_{\text{qui}}$  is derived from the broad Gaia  $G$ -band. As a result, objects tend to be brighter in  $M_{\text{qui}}$  than in  $M_{\text{max}}$ .

## Appendix 2 Classifier for the weather condition

As discussed in Section 2.4, we automatically evaluate weather conditions using images captured by the all-sky monitor camera at our observatory. In this section, we provide details on the CNN classifier developed for this purpose.

The training data set comprises 70659 nighttime sky images captured between 15 November 2021 and 16 August 2023. These original RGB color images, each with dimensions of  $600 \times 600$  pixels, were taken using an optical camera. An example of these images is presented in Figure 12. To preprocess the images, we initially trim the outer sections, creating  $400 \times 400$  pixel images that only depict the sky. Subsequently, these images were resized to  $32 \times 32$  pixels. Consequently, the CNN input consists of three-color images with dimensions of  $32 \times 32 \times 3$ . Each image is labeled either "good" or "bad." The "good" label indicates minimal cloud coverage suitable for observation, while the "bad" label denotes significant cloud presence that prevents observation. The labeling process was performed manually, resulting in a dataset of 41419 "good" and 29240 "bad" images.

Table 18 provides an overview of the CNN model used for this classification task. The model consists of two convolution layers followed by two fully connected layers. ReLU activation functions are applied to all layers, except the second fully connected layer, which plays the role of the output layer and employs the sigmoid function. To enhance the model's robustness, dropout layers were

**Table 12.** The means of the features of the training samples used for classification.

Class	$\ell$	$b$	$M_{\max}$	$M_{\text{qui}}$	$a$	$g-r$	$r-i$	$i-z$
N	4.395	-1.452	-4.201	5.322	9.716	0.679	0.349	0.281
DN	20.562	0.734	5.171	8.668	3.730	0.239	0.175	0.232
WZ	12.800	0.683	4.260	11.600	7.300	0.060	-0.033	0.230
M	7.728	-1.477	1.117	-0.394	-1.536	3.326	2.277	1.471
F	27.837	-3.261	7.822	9.377	1.815	1.165	1.245	0.646

**Table 13.** The variance-covariance matrix of the features of the training samples of class N used for classification.

	$\ell$	$b$	$M_{\max}$	$M_{\text{qui}}$	$a$	$g-r$	$r-i$	$i-z$
$\ell$	3170.073	34.244	-38.674	-4.629	17.302	0.629	4.621	2.413
$b$	34.244	110.677	4.992	1.184	-2.185	-0.109	-0.044	-0.036
$M_{\max}$	-38.674	4.992	8.928	5.405	-3.523	0.600	-0.185	0.082
$M_{\text{qui}}$	-4.629	1.184	5.405	11.549	6.144	-0.315	-0.409	-0.317
$a$	17.302	-2.185	-3.523	6.144	8.134	-0.847	-0.246	-0.348
$g-r$	0.629	-0.109	0.600	-0.315	-0.847	0.582	0.128	0.123
$r-i$	4.621	-0.044	-0.185	-0.409	-0.246	0.128	0.346	0.084
$i-z$	2.413	-0.036	0.082	-0.317	-0.348	0.123	0.084	0.204

**Table 14.** The variance-covariance matrix of the features of the training samples of class DN used for classification.

	$\ell$	$b$	$M_{\max}$	$M_{\text{qui}}$	$a$	$g-r$	$r-i$	$i-z$
$\ell$	9558.629	-68.459	9.949	-9.002	-20.457	3.363	0.883	2.055
$b$	-68.459	737.777	0.559	-1.552	-0.599	-0.292	-0.564	-0.696
$M_{\max}$	9.949	0.559	1.664	1.425	-0.238	-0.000	0.023	0.012
$M_{\text{qui}}$	-9.002	-1.552	1.425	4.806	3.380	-0.056	-0.004	0.118
$a$	-20.457	-0.599	-0.238	3.380	4.344	-0.090	-0.021	0.106
$g-r$	3.363	-0.292	-0.000	-0.056	-0.090	0.329	-0.035	-0.013
$r-i$	0.883	-0.564	0.023	-0.004	-0.021	-0.035	0.219	-0.048
$i-z$	2.055	-0.696	0.012	0.118	0.106	-0.013	-0.048	0.253

**Table 15.** The variance-covariance matrix of the features of the training samples of class WZ used for classification.

	$\ell$	$b$	$M_{\max}$	$M_{\text{qui}}$	$a$	$g-r$	$r-i$	$i-z$
$\ell$	10300.169	-159.818	-2.867	3.619	-2.652	0.161	-1.338	0.682
$b$	-159.818	1175.438	0.665	-0.978	-0.009	-0.443	-1.393	-3.670
$M_{\max}$	-2.867	0.665	0.876	0.241	-0.641	0.001	-0.010	0.042
$M_{\text{qui}}$	3.619	-0.978	0.241	0.453	0.212	-0.018	-0.011	-0.039
$a$	-2.652	-0.009	-0.641	0.212	0.894	-0.002	-0.013	-0.039
$g-r$	0.161	-0.443	0.001	-0.018	-0.002	0.044	0.011	0.028
$r-i$	-1.338	-1.393	-0.010	-0.011	-0.013	0.011	0.088	0.018
$i-z$	0.682	-3.670	0.042	-0.039	-0.039	0.028	0.018	0.270

**Table 16.** The variance-covariance matrix of the features of the training samples of class M used for classification.

	$\ell$	$b$	$M_{\max}$	$M_{\text{qui}}$	$a$	$g-r$	$r-i$	$i-z$
$\ell$	7404.059	112.985	59.471	13.047	-45.318	10.062	5.469	2.198
$b$	112.985	192.225	2.933	-0.729	-3.972	0.174	0.010	0.528
$M_{\max}$	59.471	2.933	7.396	2.052	-5.344	0.775	0.569	0.275
$M_{\text{qui}}$	13.047	-0.729	2.052	1.989	-0.063	0.184	0.332	0.118
$a$	-45.318	-3.972	-5.344	-0.063	5.279	-0.557	-0.264	-0.140
$g-r$	10.062	0.174	0.775	0.184	-0.557	2.506	-0.556	-0.030
$r-i$	5.469	0.010	0.569	0.332	-0.264	-0.556	1.303	0.041
$i-z$	2.198	0.528	0.275	0.118	-0.140	-0.030	0.041	0.231

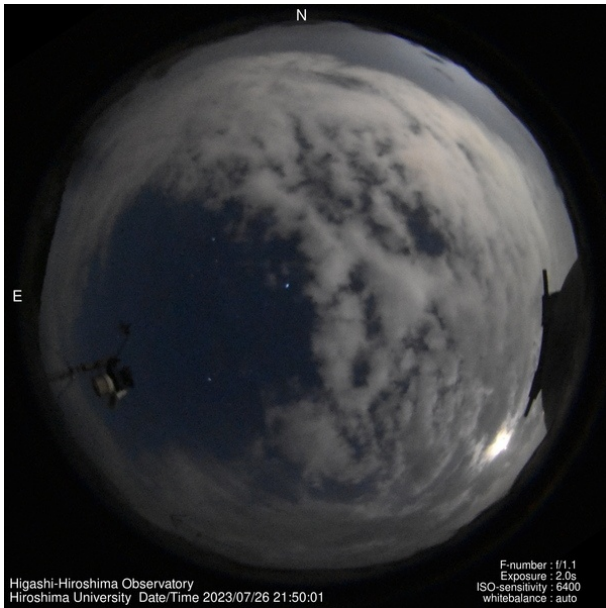


**Table 17.** The variance-covariance matrix of the features of the training samples of class F used for classification.

	$\ell$	$b$	$M_{\max}$	$M_{\text{qui}}$	$a$	$g-r$	$r-i$	$i-z$
$\ell$	14952.701	-821.461	-24.930	-66.631	-42.921	-4.859	-15.800	-8.642
$b$	-821.461	1216.280	5.908	9.737	9.813	1.150	3.017	1.538
$M_{\max}$	-24.930	5.908	5.896	6.024	0.128	0.443	1.080	0.511
$M_{\text{qui}}$	-66.631	9.737	6.024	9.210	3.186	0.626	1.723	0.850
$a$	-42.921	9.813	0.128	3.186	4.288	0.174	0.611	0.397
$g-r$	-4.859	1.150	0.443	0.626	0.174	0.130	0.093	0.061
$r-i$	-15.800	3.017	1.080	1.723	0.611	0.093	0.421	0.142
$i-z$	-8.642	1.538	0.511	0.850	0.397	0.061	0.142	0.138

**Table 18.** CNN architecture.

Layer type	Filter/Pooling size	No. of units	Output size	No. of parameters
Input	—	—	$32 \times 32 \times 3$	—
Convolution #1	$3 \times 3 \times 3$	32	$30 \times 30 \times 32$	896
Max pooling #1	$2 \times 2$	—	$15 \times 15 \times 32$	0
Convolution #2	$2 \times 2 \times 32$	64	$14 \times 14 \times 64$	8256
Max pooling #2	$2 \times 2$	—	$7 \times 7 \times 64$	0
Fully connected #1	—	128	128	401536
Fully connected #2	—	1	1	129

**Fig. 12.** An example of the images taken using the sky-monitor camera at the Higashi-Hiroshima Observatory.

incorporated after the second convolution layer and the first fully connected layer, both with a dropout rate of 0.5.

The model was optimized using the training data. The cost function used was cross-entropy and the optimization algorithm used was ADAM (Kingma, Ba 2014). A batch size of 256 was applied and 20% of the training data was reserved for validation purposes. The optimization process completed when there was no improvement in the accuracy of the validation data for 10 consecutive steps.

We acquired additional 24271 sky images from 12 October 2023 to 12 September 2024, to evaluate the generalized performance of the optimized model. Table 19 presents the confusion matrix for this test data sets, with values in parentheses corresponding to those for the training data. The accuracy for the test

**Table 19.** Confusion matrix of the weather classifier.

Pred.	Label	
	good	bad
Good	13664 (40803)	277 (288)
Bad	321 (616)	10009 (28952)
Accuracy	0.977 (0.985)	0.973 (0.990)

data is 0.975, comparable to the training data accuracy of 0.987. The confusion matrix for the test data exhibits similar features to that of the training data, suggesting no significant overfitting to the training dataset. The classifier accuracy is high enough for the automated observation of Smart Kanata.

## References

- Ahumada, R., Allende Prieto, C., Almeida, A., Anders, F., Anderson, S. F., Andrews, B. H., Anguiano, B., Arcodia, R., et al. 2020, *ApJS*, 249, 3
- Akitaya, H., Moritani, Y., Ui, T., Urano, T., Ohashi, Y., Kawabata, K. S., Nakashima, A., Sasada, M., et al. 2014, in *Ground-based and Airborne Instrumentation for Astronomy V*, ed. S. K. Ramsay, I. S. McLean, & H. Takami Vol. 9147 of *Society of Photo-Optical Instrumentation Engineers (SPIE) Conference Series*(San Diego: The International Society for Optical Engineering), 91474O
- Arai, A., Isogai, M., Yamanaka, M., Akitaya, H., & Uemura, M. 2015, *Acta Polytechnica CTU Proceedings*, 2, 257
- Assef, R. J., Stern, D., Noirot, G., Jun, H. D., Cutri, R. M., & Eisenhardt, P. R. M. 2018, *ApJS*, 234, 23
- Aydi, E., Chomiuk, L., Izzo, L., Harvey, E. J., Leahy-McGregor, J., Strader, J., Buckley, D. A. H., Sokolovsky, K. V., et al. 2020, *ApJ*, 905, 62
- Aydi, E., Chomiuk, L., Mikołajewska, J., Brink, J., Metzger, B. D., Strader, J., Buckley, D. A. H., Harvey, E. J., et al. 2023, *MNRAS*, 524, 1946
- Bellm, E. C., Kulkarni, S. R., Graham, M. J., Dekany, R., Smith, R. M., Riddle, R., Masci, F. J., Helou, G., et al. 2019, *PASP*, 131, 018002
- Bode, M. F. & Evans, A. 2008, *Classical Novae*. Vol. 43(Cambridge: Cambridge University Press)
- Chambers, K. C. & et al. 2017, *VizieR Online Data Catalog*, II/349
- Chomiuk, L., Linford, J. D., Yang, J., O'Brien, T. J., Paragi, Z.,

- Mioduszewski, A. J., Beswick, R. J., Cheung, C. C., et al. 2014a, *Nature*, 514, 339
- Chomiuk, L., Nelson, T., Mukai, K., Sokolowski, J. L., Rupen, M. P., Page, K. L., Osborne, J. P., Kuulkers, E., et al. 2014b, *ApJ*, 788, 130
- Dály, G., Galgóczi, G., Dobos, L., Frei, Z., Heng, I. S., Macas, R., Messenger, C., Raffai, P., & de Souza, R. S. 2018, *MNRAS*, 479, 2374
- Della Valle, M. & Izzo, L. 2020, *A&AR*, 28, 3
- Djorgovski, S. G., Donalek, C., Mahabal, A., Moghaddam, B., Turmon, M., Graham, M., Drake, A., Sharma, N., & Chen, Y. 2011, arXiv e-prints, arXiv:1110.4655
- Förster, F., Cabrera-Vives, G., Castillo-Navarrete, E., Estévez, P. A., Sánchez-Sáez, P., Arredondo, J., Bauer, F. E., Carrasco-Davis, R., et al. 2021, *AJ*, 161, 242
- Freund, S., Czesla, S., Robrade, J., Schneider, P. C., & Schmitt, J. H. M. M. 2022, *A&A*, 664, A105
- Gaia Collaboration, Vallenari, A., Brown, A. G. A., Prusti, T., de Bruijne, J. H. J., Arenou, F., Babusiaux, C., Biermann, M., et al. 2023, *A&A*, 674, A1
- Gal-Yam, A., Kasliwal, M. M., Arcavi, I., Green, Y., Yaron, O., Ben-Ami, S., Xu, D., Sternberg, A., et al. 2011, *ApJ*, 736, 159
- Gershberg, R. E., Katsova, M. M., Lovkaya, M. N., Terebizh, A. V., & Shakhovskaya, N. I. 1999, *A&AS*, 139, 555
- Groenewegen, M. & Blommaert, J. 2005, *Astronomy & Astrophysics*, 443, 143
- Han, Z., Boonruksar, S., Qian, S., Xiaohui, F., Wang, Q., Zhu, L., Dong, A., & Zhi, Q. 2020, *PASJ*, 72, 76
- Hastie, T., Tibshirani, R., & Friedman, J., 2017, *The elements of statistical learning: data mining, inference, and prediction*
- Heinze, A. N., Tonry, J. L., Denneau, L., Flewelling, H., Stalder, B., Rest, A., Smith, K. W., Smartt, S. J., & Weiland, H. 2018, *AJ*, 156, 241
- Hodgkin, S. T., Breedt, E., Delgado, A., Harrison, D. L., Leeuwen, M. V., Rixon, G., Wevers, T., Yoldas, A., et al. 2023, *Transient Name Server Discovery Report*, 2023-3372, 1
- Hodgkin, S. T., Harrison, D. L., Breedt, E., Wevers, T., Rixon, G., Delgado, A., Yoldas, A., Kostrzewa-Rutkowska, Z., et al. 2021, *A&A*, 652, A76
- Howell, S. B., Szkody, P., & Cannizzo, J. K. 1995, *ApJ*, 439, 337
- Inight, K., Gänsicke, B. T., Breedt, E., Israel, H. T., Littlefair, S. P., Manser, C. J., Marsh, T. R., Mulvany, T., Pala, A. F., & Thorstensen, J. R. 2023, *MNRAS*, 524, 4867
- Itoh, R., Utsumi, Y., Inoue, Y., Ohta, K., Doi, A., Morokuma, T., Kawabata, K. S., & Tanaka, Y. T. 2020, *ApJ*, 901, 3
- Ivezić, Ž., Kahn, S. M., Tyson, J. A., Abel, B., Acosta, E., Allsman, R., Alonso, D., AlSayyad, Y., et al. 2019, *ApJ*, 873, 111
- Jayasinghe, T., Kochanek, C. S., Stanek, K. Z., Shappee, B. J., Holoiën, T. W. S., Thompson, T. A., Prieto, J. L., Dong, S., et al. 2018, *MNRAS*, 477, 3145
- Jayasinghe, T., Stanek, K. Z., Kochanek, C. S., Shappee, B. J., Holoiën, T. W. S., Thompson, T. A., Prieto, J. L., Dong, S., et al. 2019, *MNRAS*, 486, 1907
- Kato, M. & Hachisu, I. 1994, *ApJ*, 437, 802
- Kato, M., Saio, H., & Hachisu, I. 2022, *ApJL*, 935, L15
- Kato, T. 2015, *PASJ*, 67, 108
- Kawabata, K. S., Nagae, O., Chiyonobu, S., Tanaka, H., Nakaya, H., Suzuki, M., Kamata, Y., Miyazaki, S., et al. 2008, in *Ground-based and Airborne Instrumentation for Astronomy II*, ed. I. S. McLean, & M. M. Casali Vol. 7014 of *Society of Photo-Optical Instrumentation Engineers (SPIE) Conference Series*(San Diego: The International Society for Optical Engineering), 70144L
- Kazarovets, E. 2024, *CBET*, 5365, 1
- Killestein, T., Pursiainen, M., Warwick, B., Kelsey, L., Ramsay, G., Kennedy, M. R., Kumar, A., Wickens, E., et al. 2024, *The Astronomer's Telegram*, 16858, 1
- Kingma, D. P. & Ba, J. 2014, arXiv e-prints, arXiv:1412.6980
- König, O., Wilms, J., Arcodia, R., Dauser, T., Dennerl, K., Doroshenko, V., Haberl, F., Hämmerich, S., et al. 2022, *Nature*, 605, 248
- Kuminski, E. & Shamir, L. 2016, *ApJS*, 223, 20
- Livio, M. 1992, *ApJ*, 393, 516
- Mahabal, A., Djorgovski, S. G., Turmon, M., Jewell, J., Williams, R. R., Drake, A. J., Graham, M. G., Donalek, C., Glikman, E., & Palomar-QUEST Team 2008, *Astronomische Nachrichten*, 329, 288
- Matheson, T., Stubbs, C., Wolf, N., Lee, C.-H., Narayan, G., Saha, A., Scott, A., Soraisam, M., et al. 2021, *AJ*, 161, 107
- Matsunaga, N., Fukushi, H., & Nakada, Y. 2005, *Monthly Notices of the Royal Astronomical Society*, 364, 117
- McMahon, R. G., Irwin, M. J., & Maddox, S. J. 2000, *The APM-North Catalogue*, *VizieR On-line Data Catalog: I/267*.
- Munari, U., Dallaporta, S., Vagnozzi, A., Maitan, A., Fiorucci, M., & Albanese, I. 2024a, *The Astronomer's Telegram*, 16769, 1
- Munari, U., Farina, A., Maitan, A., Dallaporta, S., & Andreoli, V. 2024b, *The Astronomer's Telegram*, 16727, 1
- Muthukrishna, D., Narayan, G., Mandel, K. S., Biswas, R., & Hložek, R. 2019, *PASP*, 131, 118002
- Osaki, Y. 1996, *PASP*, 108, 39
- Osaki, Y. & Meyer, F. 2002, *A&A*, 383, 574
- Schlafly, E. F. & Finkbeiner, D. P. 2011, *ApJ*, 737, 103
- Secrest, N. J., Dudik, R. P., Dorland, B. N., Zacharias, N., Makarov, V., Fey, A., Frouard, J., & Finch, C. 2015, *ApJS*, 221, 12
- Shen, K. J. & Quataert, E. 2022, *ApJ*, 938, 31
- Sinnott, R. W. 1988, *NGC 2000.0: The Complete New General Catalogue and Index Catalogues of Nebulae and Star Clusters by J. L. E. Dreyer*(Cambridge: Sky Publishing Corporation and Cambridge University Press)
- Smith, K. W., Smartt, S. J., Young, D. R., Tonry, J. L., Denneau, L., Flewelling, H., Heinze, A. N., Weiland, H. J., et al. 2020, *PASP*, 132, 085002
- Smolčić, V. 2009, *ApJL*, 699, L43
- Solheim, J. E. 2010, *PASP*, 122, 1133
- Starrfield, S., Iliadis, C., & Hix, W. R. 2016, *PASP*, 128, 051001
- Strader, J., Urquhart, R., Craig, P., Aydi, E., Chomiuk, L., Sokolovsky, K., Stanek, K. Z., Kochanek, C. S., & Shappee, B. J. 2024, *The Astronomer's Telegram*, 16550, 1
- Taguchi, K., Maeda, K., Maehara, H., Tajitsu, A., Yamanaka, M., Arai, A., Isogai, K., Shibata, M., et al. 2023, *ApJ*, 958, 156
- Tampo, Y. 2024, *The Astronomer's Telegram*, 16808, 1
- Tampo, Y., Isogai, K., Kojiguchi, N., Maehara, H., Taguchi, K., Kato, T., Kimura, M., Wakamatsu, Y., et al. 2021, *PASJ*, 73, 753
- Tonry, J. L., Denneau, L., Heinze, A. N., Stalder, B., Smith, K. W., Smartt, S. J., Stubbs, C. W., Weiland, H. J., & Rest, A. 2018, *PASP*, 130, 064505
- Tonry, J. L., Stubbs, C. W., Lykke, K. R., Doherty, P., Shivvers, I. S., Burgett, W. S., Chambers, K. C., Hodapp, K. W., et al. 2012, *ApJ*, 750, 99
- Uemura, M. & Nakaoka, T. 2024, *The Astronomer's Telegram*, 16521, 1
- Warner, B. 1995, *Cataclysmic variable stars*. Vol. 28(Cambridge: Cambridge University Press)
- Watson, C. L., Henden, A. A., & Price, A. 2006, *Society for Astronomical Sciences Annual Symposium*, 25, 47
- Yamanaka, M., Uemura, M., Kawabata, K. S., Fujii, M., Tanabe, K., Imamura, K., Komatsu, T., Arai, A., et al. 2010, *PASJ*, 62, L37
- Yao, Y., Liu, C., Deng, L., de Grijs, R., & Matsunaga, N. 2017, *ApJS*, 232, 16
- Zacharias, N., Monet, D. G., Levine, S. E., Urban, S. E., Gaume, R., & Wycoff, G. L. 2004, in *American Astronomical Society Meeting Abstracts Vol. 205 of American Astronomical Society Meeting Abstracts*(Washington, D.C.: American Astronomical Society), 48.15
- Zari, E., Hashemi, H., Brown, A. G. A., Jardine, K., & de Zeeuw, P. T. 2018, *A&A*, 620, A172
- Zhao, J. & Gao, X. 2024a, *Transient Name Server Classification Report*, 2024-14, 1
- Zhao, J. & Gao, X. 2024b, *Transient Name Server Classification Report*, 2024-2469, 1